ELSEVIER

Contents lists available at ScienceDirect

Journal of Computational Physics

www.elsevier.com/locate/jcp



A correction scheme for wall-bounded two-way coupled point-particle simulations



Pedram Pakseresht^a, Mahdi Esmaily^b, Sourabh V. Apte^{a,*}

- ^a School of Mechanical, Industrial and Manufacturing Engineering, Oregon State University, Corvallis, OR 97331, USA
- ^b Sibley School of Mechanical and Aerospace Engineering, Cornell University, Ithaca, NY 14853, USA

ARTICLE INFO

Article history: Received 20 February 2020 Received in revised form 6 July 2020 Accepted 7 July 2020 Available online 20 July 2020

Keywords: Wall-bounded flows Euler-Lagrange Point-particle approach Stokeslet solution Wall effects

ABSTRACT

The accuracy of Euler-Lagrange point-particle models employed in particle-laden fluid flow simulations depends on accurate estimation of the particle force through closure models. Typical force closure models require computation of the slip velocity at the particle location, which in turn requires accurate estimation of the undisturbed fluid velocity. Such an undisturbed velocity is not readily available when the fluid and particle phases are two-way coupled, due to the disturbance created by the particle's force in the nearby fluid velocity field. A common practice is to use the disturbed velocity to compute the particle force which can result in errors as much as 100% in predicting the particle dynamics. In this work, a correction scheme is developed that facilitates accurate estimation of the undisturbed fluid velocity in particle-laden fluid flows with and without no-slip walls. The model is generic and can handle particles of different size and density, arbitrary interpolation and projection functions, anisotropic grids with large aspect ratios, and wallbounded flows. The present correction scheme is motivated by the recent work of Esmaily & Horwitz (JCP, 2018) on unbounded particle-laden flows. Modifications necessary for wallbounded flows are developed such that the undisturbed fluid velocity at any wall distance is accurately recovered, asymptotically approaching the result of unbounded schemes for particles far away from walls. A detailed series of verification tests was conducted on settling velocity of a particle in parallel and perpendicular motions to a no-slip wall. A range of flow parameters and grid configurations; involving anisotropic rectilinear grids with aspect ratios typically encountered in particle-laden turbulent channel flows was considered in detail. When the wall effects are accounted for, the present correction scheme reduces the errors in predicting the near-wall particle motion by one order of magnitude smaller values compared to the unbounded correction schemes.

© 2020 Elsevier Inc. All rights reserved.

1. Introduction

Particle-laden flows are widely encountered in biology, nature and industry. Stroke by embolic particles in brain arteries [1], motion of red blood cells and margination of platelets in vessels [2], drug delivery, urban pollutant and settling in human respiratory system, spray combustion [3], particle-based solar receivers [4], surgical site infection caused by dispersion of squames in the operating rooms [5], sediment transport [6]; among others are examples of such flows. Understanding the

^{*} Corresponding author.

E-mail addresses: pakserep@oregonstate.edu (P. Pakseresht), me399@cornell.edu (M. Esmaily), Sourabh.Apte@oregonstate.edu (S.V. Apte).

underlying physics of such flows, making predictions without performing expensive experiments, and ultimately optimizing the current systems require accurate predictive modelling tools.

The point-particle (PP) approach [7,8] has received much attention in simulating these flows due to its simplicity and affordability. This approach was initially introduced for modelling dilute particle-laden flows with relatively small size particles that have negligible effects on the background flow. For such a "one-way" coupled flow [9], imposing the no-slip boundary condition on the surface of particles is not needed as the perturbation generated at the particle scale is insignificant. The fluid phase is solved using an Eulerian framework while particles are treated as Lagrangian points in the flow and tracked following Newton's second law of motion based on the available forces acting on them. Such one-way coupled simulations are mostly used for particle tracking and clustering. Nevertheless, owing to its affordability, this Euler-Lagrange (EL) approach has also been applied to particulate flows with dense loading or those with relatively large size particles wherein the effect of particles on the background flow is inevitable [10,11]. For such two-way coupled flows, the effect of particles on the carrier phase is modelled by applying the particle reaction force to the background flow through a momentum source term. Using such a simplified point force in modelling the inter-phase interactions, however, could result in some inaccuracies in capturing the experimental observations [12–14] or predicting the available analytical solutions [15] of particle-laden flows.

One source of inaccuracy is that, the fluid phase equations in this approach are solved for the entire flow field including the volumes occupied by the particles, and the fluid mass that is displaced by the particles is not accounted for. Several works have shown the considerable effects of this displacement and have argued that this effect should be included in addition to the point-particle force [16–19], in order to improve the predictions compared to the experimental observations. Another important source of inaccuracy, that is the focus of this work, is that the accuracy of PP in predicting the particle force can decay when the two phases are two-way coupled, owing to the disturbance created by the particle force on the background flow. Such a disturbance produces an error in the force calculations since the closure models often rely on the slip velocity computed based on the *undisturbed* fluid flow, which is not readily available in the two-way coupled simulations.

Few schemes have been recently developed as a substitute for the standard PP approach in order to improve the modelling of particle-laden flows. Pan and Banerjee [15] were the first to develop a velocity-disturbance-model that couples two phases through the velocity field rather than the momentum exchange force. Their model is valid for flows with small particle Reynolds number wherein the flow field generated around the particle is analytically known through the Stokes solution. They showed that in order to couple the two phases and capture the particle's effect on the background flow, one can directly superimpose the Stokes solution to the undisturbed fluid velocity around the particle. Their model is valid for both unbounded and wall-bounded flows since the Stokes solution for both scenarios are available. Although such a velocity-disturbance-model eliminates any dependency to the undisturbed fluid velocity and results in more accurate inter-phase coupling, it is limited to small particle Reynolds number cases. [20] introduced an alternative scheme that approximately satisfies the no-slip boundary condition at the particle surface, that is suitable for flows with relatively large size particles. In their force-coupling model, the presence of particles on the flow is approximated by a multipole expansion of a regularized steady Stokes solution. Despite its promising results for unbounded flows, for wall-bounded regimes, it requires higher order terms, more than monopole and dipole, for accurately capturing the wall lubrication effect [21], which in turn adds more complexity to their formulation. In addition, similar to [15] scheme, the assumption of Stokesian regime for flow around the particle limits the application of their method to flows with $Re_p < O(0.1)$.

Recently, efforts have been made in order to improve the accuracy of the standard PP approach by retrieving the undisturbed fluid velocity from the available disturbed field. [22] regularized the PP approach for the unbounded flows by deriving analytical equations to remove the self-induced velocity disturbance created by the particles. Their approach requires considerable computational resources to resolve the stencil over which the particle force is distributed using a Gaussian filter function. [23,24] originated a method to obtain the undisturbed field based on the enhanced curvature in the disturbed velocity field for particle Reynolds numbers of $Re_p < 10.0$. A C-field library data was built using reverse engineering technique that should be added to the current EL-PP approaches for recovering the undisturbed velocity. Although their model showed excellent agreement in the predictions of particle settling velocity and decaying isotropic turbulence [25], it is limited to (i) isotropic computational grids, (ii) particle-laden flows with particles with the maximum size of the grid and (iii) the unbounded regimes. [26] derived an analytical expression for recovering the undisturbed velocity in the unbounded regimes based on the steady state Stokes solution that was derived as the solution of a feedback force distributed to the background flow using a Gaussian smoothening. Although their model accounts for the mass displacement by the particles, it is limited to unbounded flows with small Re_p .

In a generic approach, [27] originated a correction scheme in which each computational cell, that is subjected to the two-way coupling force, is treated as a solid object that is immersed in the fluid and dragged at a velocity identical to the disturbance created by the particle. In their physics-based model, the disturbance created in each computational cell is obtained by solving the Lagrangian motion of the cell concurrently with the equation of motion of the particle. Although their model was devised to handle (i) relatively large size particles (Λ >1), (ii) isotropic and anisotropic rectilinear grids, (iii) flows with finite Re_p , and (iv) arbitrary interpolation and projection functions, it is limited to unbounded flows. [28] developed a model based on analytical and empirical equations that corrects the PP approach for Re_p <200. Following their scheme, analogous model was developed by [29] for retrieving the undisturbed temperature that is required for the interphase heat transfer computations of heated particle-laden flows. Although their velocity and temperature models account

for the mass displacement by the particles (similar to [26]) and are built for a wide range of particle Reynolds number and Peclet number, they are derived for unbounded flows only, and based on a specific filter function; namely Gaussian, that limits their applicability.

Nearly all available correction schemes have been originated and developed for the unbounded particle-laden flows. Due to the wide range of wall-bounded applications, developing more general correction schemes that are applicable for flows near solid boundaries is necessary. [30–32] underscored the need for such general correction scheme. Unique modelling issues arise in wall-bounded particulate flows that need to be addressed in any correction scheme. First, particles near a wall, specially in a turbulent flow, are relatively bigger than the grid size in wall-normal direction, and their disturbance is expected to be strong. Second, the correction scheme should be able to handle the near wall anisotropic grid resolution typically encountered in wall-bounded turbulent flows. Third, unlike unbounded flows, the disturbance created by a particle near the wall is conceptually asymmetric and should decay faster toward the wall, in order to satisfy the no-slip boundary condition. These criteria necessitate the need for a correction scheme that can capture any type of disturbance in the presence or absence of no-slip walls. [33] for the first time developed such a correction scheme that is a wall-modified extension of the Exact Regularized Point-Particle (ERPP) scheme introduced by [22]. This model was used to study the turbulence modulation in a particle-laden turbulent pipe flow.

In this paper, a new correction scheme that meets the criteria mentioned above is presented. It is conjectured that this scheme will potentially enable more accurate predictions of wall-bounded, particle-laden flows. This model is an extension of the correction scheme originated by [27] (hereinafter named as E&H) to account for the wall effects on the disturbance field in the presence of a no-slip boundary condition. Additional adjustments are made due to the collocated grid arrangement used in this study. The present scheme can be implemented and applied to flows with different rectilinear grid resolutions, arbitrary interpolation/projection functions and varying particle to grid size. For complex arbitrary shaped unstructured grids, or walls with curvature, corner or roughness, one can extend the present scheme, however, the details are left to future works. How much the disturbance field near a no-slip wall is deviated from its unbounded counterpart and how this affects the particle's motion, are the questions that we tend to address in this paper.

The paper is organized as follows. We describe our correction scheme in section 2. Correction factors due to the presence of a no-slip wall are introduced and the model is expanded to a wide range of rectilinear grid resolutions commonly encountered in wall-bounded particle-laden turbulent flows. Section 3 validates the model on predicting the velocity of a single particle settling in an unbounded domain. Then, the model will be tested for velocity of a single particle moving parallel to a wall at various wall-normal distances. In addition, the perpendicular motion of a particle toward the wall is examined to assess the model for disturbances created in the wall-normal direction. To quantify the accuracy of the model for a wide range of applications, different flow parameters as well as various anisotropic grid resolutions are investigated. In order to highlight the importance and the need for the present correction scheme, the results are compared with the unbounded version of the present model, wherein wall effects are ignored, as well as the uncorrected scheme, wherein no correction is performed. Section 4 concludes the paper with final remarks and summary of the work.

2. A correction scheme

In this section, we first introduce the main underlying issue in the two-way coupled point-particle (PP) approach, then present a methodology to resolve the issue in the presence and absence of the no-slip walls. In the standard PP approach, particles are assumed spherical and subgrid (smaller than the grid resolution), and tracked individually in a Lagrangian framework using Newton's second law as,

$$m_p \frac{du_p^{(i)}}{dt} = F^{(i)} + m_p (1 - \frac{\rho_f}{\rho_p}) g^{(i)},$$
 (1)

wherein the particle velocity in direction i, $u_p^{(i)}$, with mass of m_p is obtained using the total force of $F^{(i)}$ acting over the particle as well as its weight including buoyancy, $m_p(1-\rho_f/\rho_p)g^{(i)}$, with ρ_f and ρ_p being the fluid and particle densities, respectively. Depending upon the regime under consideration, different forces such as steady stokes drag, $F_d^{(i)}$, added mass, $F_a^{(i)}$, history effect, $F_h^{(i)}$ [7], as well as shear-induced lift, $F_l^{(i)}$ [34], Magnus effect, $F_m^{(i)}$ [35], and other forces may be included in the calculation of $F^{(i)}$,

$$F^{(i)} = F_d^{(i)} + F_a^{(i)} + F_h^{(i)} + F_h^{(i)} + F_m^{(i)} + \dots,$$
(2)

to accurately capture the particle's motion. Most of these forces are derived for a setting in which the upstream flow field is known and unaffected by the presence of particle. As an example, the steady state Stokes drag force over a sphere with diameter of d_p and in a fluid with dynamic viscosity of μ is

$$F_d^{(i)} = 3\pi \,\mu d_p \left(u_f^{(i)} - u_p^{(i)} \right),\tag{3}$$

which is analytically derived based on the relative velocity between the *undisturbed* (upstream) fluid velocity, $u_f^{(i)}$, and the particle velocity of $u_p^{(i)}$. When the two phases are one-way coupled, i.e., particles do not affect the background flow [9],

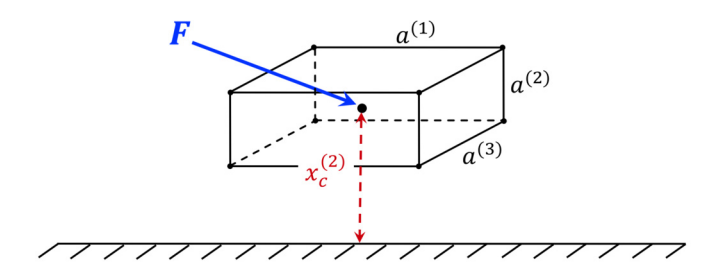


Fig. 1. A computational cell with an arbitrary size of $[a^{(1)}, a^{(2)}, a^{(3)}]$ and wall-normal distance of $x_c^{(2)}$ that is disturbed by force of **F**.

this force is used for tracking the particle to obtain its velocity and position as a function of time. In such a scenario, the particle force is not exerted to the flow and the fluid phase remains undisturbed. This process yields an accurate (and consistent with the closure model) computation of $u_f^{(i)}$, and thereby Eqs. (1) and (3). In contrast, when the two phases are two-way coupled, this force, with the same magnitude and opposite direction, is applied back to the background flow to capture the inter-phase momentum interaction. This inter-phase coupling disturbs the fluid velocity around the particle and the newly disturbed velocity, $u_d^{(i)}$, that is different from the undisturbed velocity, $u_f^{(i)}$, is used in the calculation of the drag force for the next time step. This force computed based on the disturbed fluid velocity is inaccurate and yields erroneous trajectory of the particle as well as wrong inter-phase momentum interaction. For simple canonical particle-laden flows that are not bounded, this inaccuracy depends on flow parameters such as (i) particle diameter to the grid size ratio (Λ), (ii) the choice of interpolation and projection functions used in the PP approach, (iii) particle Reynolds number and (iv) particle Stokes numbers [23,27]. Computing the undisturbed fluid velocity might be easy for some simple flows such as settling of a particle in a quiescent flow, as the unaffected field could be readily obtained from the upstream condition. However, for more complex flows with large number of particles, particularly in wall-bounded regimes, such a naive remedy becomes invalid due to the fact that the whole flow field is disturbed. This issue necessitates development of a unified scheme to accurately recover the undisturbed fluid velocity in both unbounded and wall-bounded flows. The basic concept behind development of such a scheme is described below.

Since the disturbed fluid velocity in a two-way coupled PP approach arises from a point-force, finding the disturbance created by this force can be used to correct the disturbed flow and obtained the undisturbed fluid velocity. In other words, after a point force is applied to fluid within a computational cell in a discretized domain, what is the cell fluid velocity (let us denote it by $u_c^{(i)}$) generated by this force, and what does it depend upon are the main questions under consideration. The $u_c^{(i)}$ is the velocity that is missing in the traditional two-way coupled PP approaches, and if found, could be added to the disturbed fluid velocity to obtain the undisturbed velocity as,

$$u_f^{(i)} = u_d^{(i)} - u_c^{(i)}. (4)$$

Thus, any predictive scheme that can model $u_c^{(i)}$, would be able to recover the undisturbed fluid velocity. The correction scheme presented here is based on this concept and predicts this velocity as a response of the computational cell to the particle force.

To obtain a correction scheme that is applicable to both unbounded and wall-bounded particle-laden flows, consider a computational cell in an anisotropic, homogeneous rectilinear grid, that has an arbitrary size of $[a^{(1)}, a^{(2)}, a^{(3)}]$ and located near a no-slip wall, at a wall-normal distance of $x_c^{(2)}$, as shown in Fig. 1. Note that we use rectilinear grid in this study, however, the concept explained here can be extended to arbitrary shaped unstructured grids with complex boundaries, but the details are left to future works. Hereinafter, the superscripts (1) and (3) are employed for the fluid phase streamwise and spanwise directions, respectively, while, (2) denotes the wall-normal direction. A force of $F^{(i)}$ representative of the particle force is applied to the centre of the computational cell. Conceptually, the time dependent velocity created by this force could be approximated as

$$u_c^{(i)}(t) \approx f(a^{(1)}, a^{(2)}, a^{(3)}, F^{(i)}, t, \chi_c^{(2)}).$$
 (5)

By varying the grid aspect ratio, the distance to the wall, and the amount of point-force applied, a data-set for the disturbance velocity of the computational cell as a function of time can be generated. Although finding a generic function for this data set may require some advanced data-science techniques, this relationship can be significantly simplified by applying a small force that limits us to the creeping/Stokes flow regime. For a small force and in the steady state condition, the velocity of the computational cell is linearly proportional to the force, i.e., $u_c^{(i)} \propto F^{(i)}$, and one can write it as a function of the cell dimensions and its wall distance, i.e., $u_c^{(i)} = F^{(i)}g(a^{(1)}, a^{(2)}, a^{(3)}, x_c^{(2)})$. This hypothesis is examined for a computational cell with an arbitrary size and situated at an arbitrary wall distance. A small force is applied to this cell and its velocity as a function of time is measured. From scaling analysis [36], it can be shown $|F| \ll \nu \mu$, with ν being fluid kinematic viscosity, would satisfy the infinitesimal force requirement, a condition that translates to a small Reynolds number for

the computational cell. Regardless of size and the location of the cell, it is observed that the cell velocity increases till it reaches a value with nearly negligible change in its acceleration, approximately similar to the settling velocity of a spherical particle under gravity and in the presence of a drag force. Motivated by this observation and following [27], we model the computational cell as a solid object that is subjected to the particle force $F^{(i)}$, and dragged through the surrounding computational cells. At steady state, the particle force and the drag force exerted by the surrounding computational cells balance each other and the computational cell velocity becomes only a function of its size and wall distance. The general form of the model can then be written using a first-order ordinary differential equation for the computational cell velocity, including the unsteady effect as,

$$\frac{3}{2}m_c\frac{du_c^{(i)}}{dt} = -3\pi\,\mu d_cK_t^{(i)}u_c^{(i)} - F^{(i)},\tag{6}$$

where d_c is the volume-equivalent diameter of the computational cell $(d_c = \sqrt[3]{(6/\pi)a^{(1)}a^{(2)}a^{(3)}})$ with mass of $m_c = (\pi/6)\rho_f d_c^3$. The term on the left hand side expresses the unsteady effect of the force on the computational velocity wherein the prefactor 3/2 captures the added mass effect. The first term on the right hand side of the equation, $3\pi\mu d_c K_t^{(i)}u_c^{(i)}$, is the Stokes drag force acting on the computational cell by its surrounding cells wherein the relative velocity is $-u_c^{(i)}$ as the ambient flow for the disturbance field is at rest. The adjustment to the Stokes drag is expressed by the factor $K_t^{(i)}$ as,

$$K_t^{(i)} = \frac{K_c^{(i)} C_r}{K_n^{(i)} C_t^{(i)}}.$$
 (7)

Here, $K_c^{(i)}$ accounts for non-sphericity of the computational cell and depends on its size and aspect ratio. The factor $K_p^{(i)}$ accounts for wall effects as well as the interpolation and projection functions commonly employed in PP approach. The factor C_r accounts for the non-linear finite force effect (or the finite Reynolds number effect for the computational cell) whereas $C_t^{(i)}$ considers the limited exposure time of the particle force to the computational cell. These geometric and physics-based factors are defined and explained in details in the following subsections after the numerical method is explained below. Concerning the corresponding empirical expressions obtained in the following subsections, we looked at the behaviour of the data and tried to find the most relevant functions that could capture such behaviour.

2.1. Numerical method

Details on the numerical method employed in this study can be found in [37,38], thus only a brief description is given here. The fluid phase momentum and continuity equations are solved using a pressure-based, second-order, fractional time stepping scheme on a collocated grid arrangement with the velocity and pressure stored at the centroid of the control volumes. For computations of this section, a source term representative of the force is added to the momentum equation of the control volume wherein the force disturbs the fluid phase. The cell-centred fluid velocity field is advanced by solving the momentum equations as a predictor step. The predicted velocities are interpolated to the faces and then projected to satisfy the continuity constraint. Projection yields the pressure potential at the cell centres, and its gradient is used to correct the cell and face-normal velocities.

2.2. Geometric correction factor, K_c

The geometric correction factor, K_c , is obtained based on the fact that a moving solid object in an unbounded flow with a small Reynolds number experiences a constant drag coefficient that is dependent on its shape and geometry [39]. Inspired by this, the geometric correction factor to the Stokes drag of the computational cell is conjectured to be a function of its geometry. In this part, an expression for K_c is derived that is different than the one derived in E&H, in order to cover a wider range of grid aspect ratios typically encountered in highly turbulent channel flows.

The procedure is explained as follows. A sufficiently large computational domain is chosen with a uniform grid resolution of 128^3 . Boundary conditions for wall-normal direction are set to be no-slip and slip to enforce wall effects while periodic boundary condition is employed for the other directions of the domain. A small and stationary force, $F_{small}^{(i)}$, that generates a disturbance field with nearly zero Reynolds number, is applied to the centre of a computational cell in i direction. Note that the computational cell is located in the middle of the domain wherein the no-slip boundary conditions have zero effect on the generated disturbance field. At steady state, the velocity of the computational cell is directly measured and $K_c^{(i)}$ is obtained by using Eq. (6) as,

$$K_{c,measured}^{(i)} = \left| \frac{F_{small}^{(i)}}{3\pi \,\mu d_c u_c^{(i)}} \right|,\tag{8}$$

with other correction factors being one by definition as the force is small $(C_r=1)$, applied only to one cell and sufficiently away from the no-slip wall $(K_p^{(i)}=1)$, and has infinite exposure time $(C_t^{(i)}=1)$. The procedure is repeated for a wide range of

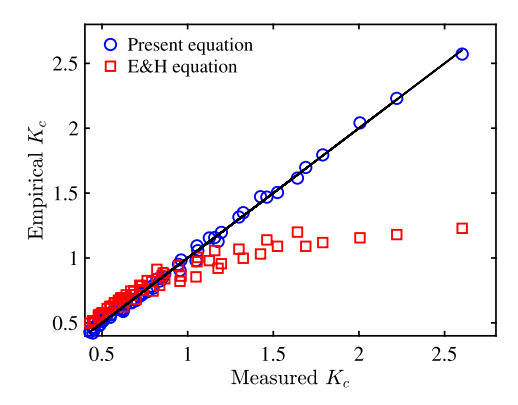


Fig. 2. Prediction of Eqs. (9) and (10) versus numerical measurements of K_c for a wide range of grid aspect ratios.

grid aspect ratio of $0.05 \sim a^{(2)}/a^{(1)} \sim 20$ and $0.1 \sim a^{(3)}/a^{(1)} \sim 10$. The choice of grid aspect ratio studied here is inspired by the grid resolution of highly turbulent channel flows [40]. A best fit to the numerically measured data is obtained as,

$$\begin{split} K_c^{(i)} &= 0.1705 \exp \left[(\Gamma_{max}^{(i)})^{-0.4005} (\Gamma_{min}^{(i)})^{0.06408} \right] (\Gamma_{max}^{(i)})^{0.7058} (\Gamma_{min}^{(i)})^{-0.452} \\ &+ \ln \left[(\Gamma_{max}^{(i)})^{-0.03746} (\Gamma_{min}^{(i)})^{0.2049} \right] (\Gamma_{max}^{(i)})^{0.355} (\Gamma_{min}^{(i)})^{0.05338}, \end{split} \tag{9}$$

where

$$\Gamma_{max}^{(i)} = \max \left\{ \frac{a^{(j)}}{a^{(i)}}, \frac{a^{(k)}}{a^{(i)}} \right\}, \quad \Gamma_{min}^{(i)} = \min \left\{ \frac{a^{(j)}}{a^{(i)}}, \frac{a^{(k)}}{a^{(i)}} \right\}; \quad j, k \neq i.$$
 (10)

Fig. 2 shows excellent prediction of the above empirical equation against our numerically measured values of $K_c^{(i)}$. Note that due to the higher aspect ratios studied in this work, larger values for $K_c^{(i)}$ are obtained compared to those reported in E&H. For the sake of comparison, the expression provided in E&H is also used to predict our measured values. Consistent with their work, for the range of $K_c^{(i)} \le 1$, their expression shows excellent prediction and nearly matches the results of our present expression as well. However, for $K_c^{(i)}$ 1 that corresponds to computational cells with higher aspect ratio studied in this work, the present expression predicts much better than that of E&H owing to the fact that the latter was calibrated only for aspect ratios within the range of $K_c^{(i)} \le 1$.

2.3. The wall and interpolation effects, K_p

The question that arises now is, how does the geometric correction factor, $K_c^{(i)}$, change when the computational cell of interest approaches the wall? The answer for this question lies in a new wall adjustment factor on geometric correction factor. In order to answer this question, we first look at the near wall motion of a spherical object wherein its drag coefficient increases closer to the wall. [41] derived an analytical equation for the wall-modified drag coefficient of a sphere moving parallel to the wall, while [42] using lubrication theory, obtained the corresponding parameter for its normal motion toward the wall. Based on these observations, it is expected that the wall adjustment on the geometric correction factor be dependent on the force direction and increases as wall-normal distance decreases. Having such a direction dependent adjustment is of importance as in wall-bounded particle-laden flows, particles interact with the near wall sweep and burst events [43], thus experiencing different forces in the two directions and disturbing the background flow differently.

Following the procedure described in the previous part for obtaining $K_c^{(i)}$, its wall adjustment is achieved by applying the point-force at various wall distances. For each wall distance Eq. (8) gives rise to a wall-modified geometric correction factor, $K_{c,w}^{(i)}$, that deviates from its unbounded counterpart, $K_c^{(i)}$. The ratio of these two yields a wall adjustment factor as,

$$\Psi_k^{(i)} = \frac{K_{c,w}^{(i)}}{K_c^{(i)}}.\tag{11}$$

This factor approaches unity for cells sufficiently away from the wall (i.e., $K_{c,w}^{(i)} = K_c^{(i)}$) and is greater than one for those near the wall. This procedure is repeated for the studied grid aspect ratios, for each of which, $\Psi_k^{(i)}$ is measured and tabulated for various wall distances. For each grid resolution and wall distance, the measurements are performed for both parallel and normal forces, separately. As explained in Appendix A, for isotropic grid resolution, it is observed that the wall adjustment to the Stokes drag coefficient of a spherical object obtained empirically by [44] matches our measured data.

This expression, however, deviates for highly skewed anisotropic grids, inevitably encountered in the wall-bounded flows. This underscores the need for a more accurate expression that could handle a wide range of grid aspect ratios. Motivated by the wall-modified drag expressions derived in [42] and [41], the best expression to fit our measured data for forces in both parallel and normal directions was found to be,

$$\Psi_k^{(i)} = 1 + \frac{A^{(i)}}{1 + B^{(i)}h_\nu^{(i)}},\tag{12}$$

where $h_k^{(i)}$ is the normalized wall distance of the centre of the computational cell k as,

$$h_k^{(i)} = \begin{cases} \frac{x_k^{(2)}}{a^{(i)}}, & i=1,3\\ \frac{x_k^{(2)}}{a^{(1)}}, & i=2 \end{cases}$$
 (13)

with $x_k^{(2)}$ being the dimensional wall distance of the computational cell k, and $A^{(i)}$ and $B^{(i)}$ are dependent on the grid aspect ratio as,

$$A^{(i)} = \begin{cases} \frac{\ln\left(26.31\frac{a^{(3)}}{a^{(1)}}\right)}{\left(0.05761 + 5.373\left(\frac{a^{(2)}}{a^{(1)}}\right)^{1.057}\right)}, & i = 1\\ \frac{\ln\left(14.04\frac{a^{(3)}}{a^{(1)}}\right)}{\left(0.06608 + 5.14\left(\frac{a^{(2)}}{a^{(1)}}\right)^{1.592}\right)}, & i = 2\\ \frac{\ln\left(26.31\frac{a^{(1)}}{a^{(3)}}\right)}{\left(0.05761 + 5.373\left(\frac{a^{(2)}}{a^{(3)}}\right)^{1.057}\right)}, & i = 3 \end{cases}$$

$$(14)$$

$$B^{(i)} = \begin{cases} \frac{\exp\left(-0.02873\frac{a^{(3)}}{a^{(1)}}\right)}{\left(0.00008 + 0.5601\left(\frac{a^{(2)}}{a^{(1)}}\right)^{1.894}\right)}, & i = 1\\ \frac{\exp\left(-1.252\frac{a^{(3)}}{a^{(1)}}\right)}{\left(0.01354 + 3.688\left(\frac{a^{(2)}}{a^{(1)}}\right)^{2.202}\right)}, & i = 2\\ \frac{\exp\left(-0.02873\frac{a^{(1)}}{a^{(3)}}\right)}{\left(0.00008 + 0.5601\left(\frac{a^{(2)}}{a^{(3)}}\right)^{1.894}\right)}, & i = 3 \end{cases}$$

$$(15)$$

As implied by Eq. (12), $\Psi_k^{(i)}$ becomes unity when the disturbance occurs sufficiently away from the wall as,

$$\lim_{h_{\nu}^{(i)} \to \infty} \Psi_k^{(i)} = 1. \tag{16}$$

It should be noted that our results show that for disturbances created by the wall-normal force applied to highly skewed grids, i.e., $a^{(2)}/a^{(3)}$ <0.5, $\Psi_k^{(i)}$ for the first computational cell attached to the wall is better predicted by,

$$\Psi_{first,cell}^{(2)} = \frac{\ln\left(25.3\frac{a^{(3)}}{a^{(1)}}\right)}{-0.0007149 + 2.364\left(\frac{a^{(2)}}{a^{(1)}}\right)^{0.7796}}.$$
(17)

Fig. 3 shows the prediction of $\Psi_k^{(i)}$ using the above equations for parallel and normal forces, separately. More than thousand measurements are included in these plots to cover the wall distances in the range of $0.5\kappa_c^{(2)}/a^{(2)}18.5$ as well as the studied grid resolutions. Note that the parallel force measurements were performed for both streamwise and spanwise directions to cover the range of grid configurations employed in these directions. Larger values correspond to the computational cells with higher aspect ratio or those situated closer to the wall. As can be inferred from Fig. 3, ignoring wall effect on the geometric correction factor and letting $\Psi_k^{(i)} = 1$ yields overprediction of the computational velocity of the cell as $u_c^{(i)} \propto (\Psi_k^{(i)} K_c^{(i)})^{-1}$. As shown later, this over prediction becomes remarkable when particles travel very close to the wall which results in erroneous particle trajectory.

So far we considered the disturbance created by a small force that is applied to the centre of a computational cell. This condition assumes that the particle force is applied only to a cell that contains the particle. However, in EL-PP simulations, this assumption does not necessarily hold, and the particle force is commonly distributed to the number of computational

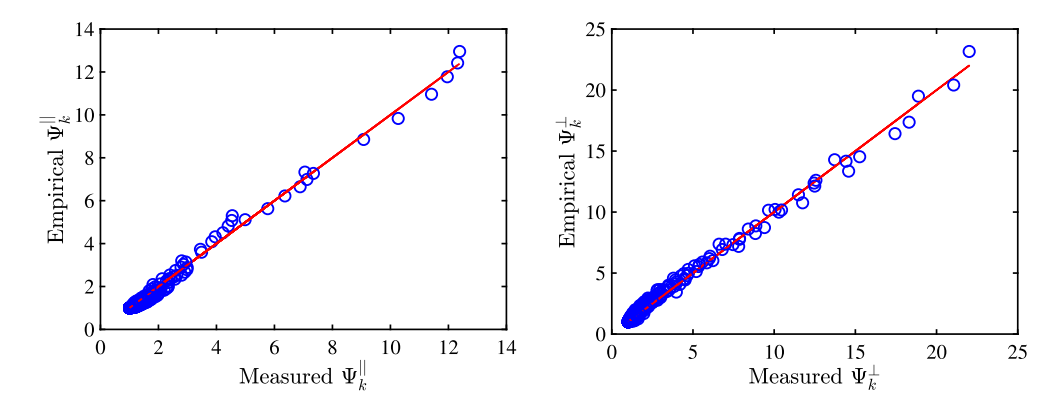


Fig. 3. Predictions of Eqs. (12)-(15) and (17) for parallel forces, i = 1, 3 (left), and wall-normal force, i = 2 (right), are shown in comparison with the numerical measurements. Results are based on the studied wall distances as well as grid resolutions.

cells that are located within the stencil of the projection function. Depending upon their distance from the force, they receive a fraction of this force and get disturbed differently. Now, in the next time step, when the fluid forces are to be computed, a function is similarly employed to interpolate the fluid quantities to the location of particle. During this process, the disturbance created in the surrounding computational cells in the previous time step will enter into the force calculations and depending on the stencil of this function, particle receives different disturbances. To accurately capturing the disturbance that particle receives, these effects must be accounted for in the correction scheme. [27] derived an analytical formulation for these effects for unbounded flows wherein the disturbance around the particle is symmetric. However, near a no-slip wall, the shape and strength of the disturbance field vary and it becomes more asymmetric. Below, we generalize the analytical expression of E&H to account for the no-slip walls and a new analytical expression is derived.

Suppose the particle force, $F_p^{(i)}$, is fed back to the background flow using a projection function that has a certain bandwidth. Those computational cells that lie within the bandwidth receive a fraction of the force depending on their distance to the particle. Accordingly, the corresponding force that computational cell i receives is expressed as,

$$F_i^{(i)} = \beta_j F_p^{(i)},$$
 (18)

where β_j is the projection coefficient (weight) corresponding to the computational cell j. When the particle forces (e.g., the drag that requires fluid velocity) are being calculated, the disturbance field is interpolated to the particle location from the neighbouring cells as,

$$u_c^{(i)} = \sum_{i=1}^{n_j} \gamma_j u_{c,j}^{(i)},\tag{19}$$

where $u_c^{(j)}$ is the disturbance that particle receives in i direction and γ_j is the interpolation coefficient corresponding to the computational cell j that has computational velocity (disturbance velocity) of $u_{c,j}^{(i)}$, n_j is the total number of adjacent computational cells that are employed for the interpolation. It is imperative to note that unlike staggered grids, in collocated arrangements, γ_j and β_k coefficients are direction independent. The question that arises here is how to compute the computational velocity of the adjacent computational cells, $u_{c,j}^{(i)}$, when they are imposed to a fraction of particle force. A naive way to obtain that, is to simply use Eq. (6) for each cell with its given force, $F_j^{(i)}$, assuming that the computational cells are independent and only disturbed by their direct forces. In practice, however, this assumption does not hold and each computational cell gets disturbed not only by its direct force but also through the perturbations induced by the adjacent cells. For instance, when the computational cell k is disturbed by its own force, $\beta_k F_p^{(i)}$, the created disturbance velocity in this cell pushes and perturbs the surrounding cells through $\alpha_{kj}^{(i)}$ that is the velocity ratio of cell j, generated by perturbation of cell k, to that of the computational cell k. This implies the fact that the disturbance created in computational cell, e.g., j, constitutes a combination of the one created by its own direct force and those created by the adjacent cells. Upon finding a closure for $\alpha_{kj}^{(i)}$, a linear superposition is valid if the created disturbance field meets the zero Reynolds number criterion. For unbounded flows and in the limit of zero Reynolds number, [27] showed that $\alpha_{kj}^{(i)}$ can be predicted using the Stokes solution that is the solution for the velocity field generated around a sphere slowly moving in an unbounded quiescent flow as,

$$\alpha_{kj}^{(i)} = \frac{3}{4} r_{kj}^{\prime - 1} \left(1 + \cos^2 \theta_{kj}^{(i)} \right) + \frac{1}{4} r_{kj}^{\prime - 3} \left(1 - 3\cos^2 \theta_{kj}^{(i)} \right), \tag{20}$$

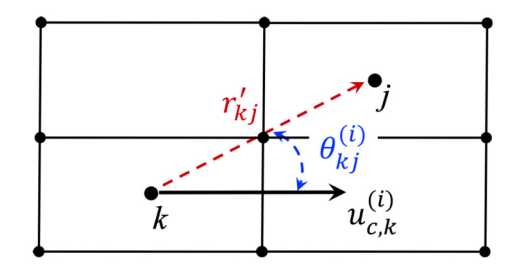


Fig. 4. Schematic of computational cell k that is disturbed by a small force and has disturbance velocity of $u_{c,k}^{(i)}$ which perturbs the adjacent computational cells through the modelled Stokes solution. r'_{kj} is the normalized distance between cell k and j with polar angle of $\theta_{kj}^{(i)}$ between the line passing through these cells and the i direction.

Table 1 Measured b_{lmn} values in comparison with the prediction of Eq. (20) normalized with the characteristic length of $0.25d_c$ and $0.28d_c$, separately. Shown also includes the corresponding measured values from [27] that are based on the staggered grid arrangement.

$a^{(2)}/a^{(1)}$	$a^{(3)}/a^{(1)}$			b_{000}	b_{100}	b ₀₁₀	b ₁₁₀	b_{001}	b_{101}	b ₀₁₁	b ₁₁₁
1.0	1.0	measured	collocated	1.0	0.31	0.27	0.18	0.27	0.18	0.16	0.14
			staggered	1.0	0.50	0.25	0.24	0.25	0.24	0.15	0.16
		predicted	using $0.25d_c$	1.0	0.45	0.24	0.25	0.24	0.25	0.17	0.18
			using $0.28d_c$	1.0	0.50	0.27	0.27	0.27	0.27	0.19	0.20
1.0	2.0	measured	collocated	1.0	0.41	0.33	0.26	0.19	0.17	0.15	0.14
			Staggered	1.0	0.62	0.33	0.34	0.17	0.18	0.13	0.15
		predicted	using $0.25d_c$	1.0	0.56	0.31	0.31	0.15	0.16	0.13	0.14
			using $0.28d_c$	1.0	0.61	0.35	0.34	0.17	0.18	0.15	0.16
2.0	4.0	measured	collocated	1.0	0.62	0.36	0.34	0.22	0.21	0.18	0.18
			staggered	1.0	0.83	0.31	0.34	0.16	0.17	0.13	0.13
		predicted	using $0.25d_c$	1.0	0.81	0.24	0.25	0.12	0.12	0.10	0.11
		-	using $0.28d_c$	1.0	0.87	0.27	0.28	0.13	0.13	0.12	0.12

where $\theta_{kj}^{(i)}$ is the polar angle between the line passing through the computational cells k and j and the i direction (Fig. 4), whereas r_{kj}' is the distance between these two cells normalized by the characteristic length of the computational cell. The choice of this equation was inspired by the fact that the computational cell is treated as a solid object that moves in the fluid and consequently disturbs the surrounding fluid in a manner similar to a solid sphere. Using the prediction of this equation and a characteristic length of $0.28d_c$, they showed an excellent agreement with their numerical measurements.

For the collocated grid arrangement used in this study, we found that Stokes solution (Eq. (20)) normalized with a smaller characteristic length of 0.25dc better predicts our numerical measurements. This was done by performing measurements similar to the previous parts. A small force in i direction is applied to the computational cell k located in the middle of a sufficiently large periodic box. At steady state, we measure the velocity of the perturbed cell k as well as those of its adjacent cells (i.e., j). The velocity ratio of these cells, $u_{c,j}^{(i)}/u_{c,k}^{(i)}$, is $\alpha_{kj}^{(i)}$ by definition. For the sake of clarity, this parameter could be alternatively denoted by b_{lmn} in which the subscript lmn corresponds to the location of cell j, that is $[la^{(1)}, ma^{(2)}, na^{(3)}]$ away from the computational cell k. As an example, b_{100} represents the velocity ratio of cell j to k with j being the immediate cell in the (1) direction and right hand side of the perturbed cell k. Table 1 shows the prediction of Eq. (20) normalized with both $0.25d_c$ and $0.28d_c$ compared to our numerical measurements on the collocated grid arrangement for different aspect ratios. Better predictions are obtained by the former characteristic length. For the sake of comparison, we have also included the corresponding values of [27] that are based on the staggered grid arrangements, revealing a slight difference between these two arrangements. The difference is justified due to the fact that in collocated arrangements, the cell-centred velocity that is commonly used for particle force computations, does not precisely satisfy the continuity equation as the face velocity does, thereby causing small errors in the results compared to those of the staggered arrangements.

The next step is to investigate how $\alpha_{kj}^{(i)}$ changes when the disturbance occurs near a no-slip wall. One could substitute this parameter with the wall-bounded Stokes solution of a sphere moving in a quiescent flow and near a no-slip wall [45,46]. Although there have been a few methods for simplifying such solution (e.g., [47]), it is expressed as expansions of spherical harmonics with the coefficients that are obtained iteratively as the solution of an infinite linear system. This makes the use of wall-bounded Stokes solution computationally expensive for EL approaches.

An alternative remedy is the choice of the "Stokeslet solution" that is the flow field generated by a point force in a quiescent fluid. Direct analytical solutions are available for both unbounded and wall-bounded flows [48] that makes it more desirable and feasible to be implemented in EL approaches. Assuming that the ratio of the wall-bounded to the unbounded Stokes solution, $\alpha_{stk,b}^{(i)}/\alpha_{stk,un}^{(i)}$, approximately equals to the corresponding ratio of Stokeslet solution, $\alpha_{stk,b}^{(i)}/\alpha_{stk,un}^{(i)}$, an analytical expression for the wall adjustment to $\alpha_{kj}^{(i)}$ is derived (see Appendix B for the detailed Stokeslet solutions) as,

$$\Phi_{kj}^{(i)} = \frac{(\alpha_{stkl,b}^{(i)})_{kj}}{(\alpha_{stkl,un}^{(i)})_{kj}} = 1 - \left[\frac{\frac{1}{|R_{kj}|} + \frac{(R_{kj}^{(i)})^2}{|R_{kj}|^3} + \frac{2x_k^{(2)}f_{kj}^{(i)}}{|R_{kj}|^6}}{\frac{1}{|r_{kj}|} + \frac{(r_{kj}^{(i)})^2}{|r_{kj}|^3}} \right], \tag{21}$$

where.

$$f_{kj}^{(i)} = (-1)^{i} \left(x_{k}^{(2)} |R_{kj}|^{3} - 3|R_{kj}|(R_{kj}^{(i)})^{2} x_{k}^{(2)} - |R_{kj}|^{3} R_{kj}^{(2)} + 3|R_{kj}|(R_{kj}^{(i)})^{2} R_{kj}^{(2)} \right); \tag{22}$$

$$r_{kj}^{(i)} = (x_j^{(i)} - x_k^{(i)}); \quad |r_{kj}| = \sqrt{\sum_{i=1}^{3} (r_{kj}^{(i)})^2}; \tag{23}$$

$$R_{kj}^{(i)} = \begin{cases} r_{kj}^{(i)}, & i = 1, 3\\ r_{kj}^{(2)} + 2x_k^{(2)}, & i = 2 \end{cases}; \quad |R_{kj}| = \sqrt{\sum_{i=1}^{3} (R_{kj}^{(i)})^2}, \tag{24}$$

and $x_j^{(i)}$ and $x_k^{(i)}$ are the i coordinate of the computational cell j and k, respectively. Note that $\Phi_{kj}^{(i)}$ is not normalized by any characteristic length which makes it general for both staggered and collocated grid arrangements. It is imperative to mention that when the disturbance created by a particle is situated sufficiently away from the wall, both bounded and unbounded Stokeslet solutions become identical and this parameter becomes unity as

$$\lim_{\substack{x_k^{(i)} \to \infty}} \Phi_{kj}^{(i)} = 1,\tag{25}$$

which makes the model robust for capturing the disturbance field created at any wall distance, a common scenario in wall-bounded particulate flows. Knowing the adjacent perturbations, now we can find the computational velocity of each cell and derive the analytical expression for $K_p^{(i)}$ as follows.

For the particle force that is stationary and distributed to its neighbour cells, in the limit of steady state and zero Reynolds number, the computational velocity of cell j is obtained as the superposition of disturbances created by its own force as well as its adjacent cells as,

$$u_{c,j}^{(i)} = \sum_{k=1}^{n_k} \left[\frac{\alpha_{kj}^{(i)} \beta_k \Phi_{kj}^{(i)}}{\Psi_k^{(i)}} \right] \frac{-F_p^{(i)}}{3\pi \mu d_c K_c^{(i)}},\tag{26}$$

where n_k is the total number of computational cells to which the particle force is distributed. In Eq. (26) and what follows, no implicit summation over repeated indices is implied. Note that the wall adjustment to the geometric correction factor, $\Psi_k^{(i)}$, is kept in the bracket as it varies among the adjacent cells, owing to their different wall-normal distances. Knowing the disturbance velocity for the computational cells around the particle, the disturbance velocity seen by the particle is obtained using Eqs. (19) and (26) as,

$$u_c^{(i)} = \sum_{j=1}^{n_j} \left[\gamma_j \sum_{k=1}^{n_k} \left[\frac{\alpha_{kj}^{(i)} \beta_k \Phi_{kj}^{(i)}}{\Psi_k^{(i)}} \right] \right] \frac{-F_p^{(i)}}{3\pi \, \mu d_c K_c^{(i)}},\tag{27}$$

where n_j is the total number of computational cells from which the fluid properties are interpolated to the particle location. The analytical expression for $K_p^{(i)}$ is then derived as

$$K_p^{(i)} = \sum_{j=1}^{n_j} \left[\gamma_j \sum_{k=1}^{n_k} \left[\frac{\alpha_{kj}^{(i)} \beta_k \Phi_{kj}^{(i)}}{\Psi_k^{(i)}} \right] \right]. \tag{28}$$

In the limit of large wall distances, since both $\Psi_k^{(i)}$ and $\Phi_{kj}^{(i)}$ approach unity, $K_p^{(i)}$ becomes identical to that of E&H which was derived for unbounded regimes. It is crucial to mention that with this formulation, all wall adjustments are accounted for in the derivation of $K_p^{(i)}$.

for in the derivation of $K_p^{(i)}$. For cases where only "box filtering" (zeroth order) is utilized, i.e., the particle only disturbs one cell from which the fluid properties are used for the particle too $(n_k=n_j=1)$, we have $\gamma_j=\beta_k=\alpha_{kj}^{(i)}=\Phi_{kj}^{(i)}=1$. In this case, $K_p^{(i)}=1/\Psi_k^{(i)}$, wherein subscript k corresponds to the cell in which the particle lies. In such a simple case, $K_p^{(i)}$ becomes only the wall effect on the correction scheme.

2.4. Correction for the finite Reynolds number, C_r

The Stokes drag used in Eq. (6) is only valid for disturbances created with zero Reynolds number. To account for the higher Reynolds number effects, a Schiller-Naumann correction factor, analogous to the finite Reynolds number adjustment to the Stokes drag of a sphere [49],

$$C_r = 1 + 0.15Re_c^{0.687},\tag{29}$$

can be used [27]; where, $Re_c = u_c d_c / v$ is defined as the Reynolds number of the computational cell based on its velocity and diameter. A wall-modified version of this equation has been empirically derived by [44], yet our results show that the use of Schiller-Naumann expression (Eq. (29)) still yields better predictions for the studied wall-bounded cases. This expression captures only the change to the magnitude of the Stokes drag for higher Re_c cases, however, the complexity of the asymmetric disturbance field at high Re_c breaks the use of Eq. (20) and the linear superposition employed in the derivation of Eq. (28). Therefore, it is argued that for high Re_c , a more elaborate formulation might be required. As explained later, the current formulation produces reasonable results for cases with Re_c of up to 10, consistent with the observations of [24]. For larger Re_c , [28] showed that the need for the correction diminishes. Although this effect is partly captured by introducing a temporal correction factor for finite exposure time, $C_t^{(i)}$, explained in the next part, a comprehensive study on the necessity of the correction scheme for a range of particle Reynolds number is left for future investigations.

2.5. Correction for the finite exposure time, C_t

A particle moving in the computational domain spends a limited time within each computational cell and disturbs the cell for a finite time. This finite time exposure of particle has to be accounted for in Eq. (6), separately. The unsteady term in this equation is considered for the unsteady effect of a stationary force and does not include the limited exposure time of this force. To demonstrate the need for this additional correction factor, consider a high velocity particle that spends an infinitesimal time in each computational cell. That infinitesimal time is not sufficient to accelerate the fluid within the computational cell, thus $\mathbf{u}_c \rightarrow 0$, obviating the need for any correction. However, Eq. (6) is formulated in a Lagrangian frame attached to the particle and is integrated concurrent with the particle's equation of motion (Eq. (1)). Thus, the recorded time is not reset with the entrance of a particle to a computational cell but monotonically increases, yielding a finite \mathbf{u}_c . The effect of finite time at which a particle passes through a computational cell is employed by $C_t^{(i)}$ as an additional correction factor.

In order to perform this correction, one could track the particle within each computational cell and only integrate Eq. (6) over the period of time that particle spends in the cell and upon its exit the force becomes zero. To avoid the complexity added by this, we use the corresponding correction factor derived in E&H as,

$$C_t^{(i)} = 1 - \frac{\tau_c^{(i)}}{\Delta t^{(i)}} \left(1 - \exp\left(-\frac{\Delta t^{(i)}}{\tau_c^{(i)}}\right) \right),\tag{30}$$

where,

$$\Delta t^{(i)} = \frac{a^{(i)}}{|u_n^{(i)}|} \quad \text{and} \quad \tau_c^{(i)} = \frac{d_c^2}{12\nu K_c^{(i)}},\tag{31}$$

where $au_c^{(i)}$ and $\Delta t^{(i)}$ are the computational cell relaxation time and the particle residence time in i direction of the computational cell, respectively. The factor $C_t^{(i)}$ is a time-average of the solution of Eq. (6) for a small force that is applied on top of a computational cell (details on the derivation of this expression can be found in E&H). Accordingly, for a high velocity particle, its exposure time to the cell becomes small, $\Delta t \to 0$ and using Eq. (30), $C_t^{(i)} \to 0$ which eliminates any need for correction. However, for slow particles, $\Delta t \to \infty$ and $C_t^{(i)} \to 1$ which enforces the correction. This is the limit that was used in the previous parts where the correction factors of $K_p^{(i)}$, $K_c^{(i)}$ and C_r were derived. In the next part, we combine all these correction factors and explain the steps in order to correct the PP approach.

2.6. The correction algorithm

The entire correction scheme reduces to the computation of Eq. (6) that is solved concurrently with the equation of motion of the particle (Eq. (1)). Although one could simply use any time integration scheme for these two equations, we use an explicit method for the results presented in this work. Therefore, knowing the $u_c^{(i)}$ and $u_p^{(i)}$ from the previous time step, the following procedure is used.

- 1. Compute the disturbed velocity at the location of particle, $u_d^{(i)}$, that is readily available in the standard PP packages.
- 2. Compute the undisturbed velocity at the location of particle, $u_f^{(i)}$, by using Eq. (4) and having the computational velocity

at the location of particle, $u_c^{(i)}$.

- 3. Compute the total fluid force exerted at the location of particle, $F^{(i)}$.
- 4. Update the velocity of particle, $u_p^{(i)}$, using Eq. (1).
- 5. Calculate $K_c^{(i)}$ using Eqs. (9) and (10) based on the grid size $[a^{(1)}, a^{(2)}, a^{(3)}]$ in which particle is located. 6. Identify the location of surrounding cells to which the particle force is distributed (n_k) .
- 7. Identify the location of surrounding cells from which the fluid quantities are interpolated to the location of particle (n_j) .
- 8. From the location of particle to the above computational cells, calculate r'_{kj} and $\theta^{(i)}_{kj}$ and thereby $\alpha^{(i)}_{kj}$ using Eq. (20).
- 9. In the presence of no-slip walls, calculate $\Phi_{kj}^{(i)}$ and $\Psi_{k}^{(i)}$ based on Eqs. (12)-(15) and Eqs. (21)-(24), respectively. 10. Compute $K_p^{(i)}$, using Eq. (28) and knowing β_k , γ_j , $\alpha_{kj}^{(i)}$, $\Phi_{kj}^{(i)}$ and $\Psi_k^{(i)}$. 11. Compute Re_c and thereby C_r using Eq. (29). 12. Compute $T_c^{(i)}$ and $T_c^{(i)}$ and $T_c^{(i)}$ using Eq. (31) and thereby $T_c^{(i)}$ using Eq. (30). 13. Compute $T_c^{(i)}$ using Eq. (7) by knowing $T_c^{(i)}$, $T_c^{($

- 14. Update $u_c^{(i)}$ using Eq. (6).

The initial condition for the procedure above is $u_c^{(i)} = 0$ as before injecting particles into the domain, the fluid phase is undisturbed. However, when particles leave the computational cells, the $u_c^{(i)}$ does not become zero as the disturbance will propagate to adjacent cells before a particle enters the neighbouring cells. For isotropic grids, the simplified formulation introduced in Appendix A could be used to compute $\Psi_k^{(i)}$ in step 9 above. It is imperative to mention that for particle-laden flows wherein the particle time step is smaller than that of the fluid, sub-cycling for particles' motion is typically performed; for example to accurately account for inter-particle collisions [6,50]. Particles using their time step are advanced during the frozen flow time step, then at the end of the sub-cycling, their force will be applied to the background flow. For such cases, the correction velocity is computed once the sub-cycling is finished as that is when the flow is altered by the particles' force. For particle-laden flows with multiple particles in each cell, the current formulation solves the $u_c^{(i)}$ equation for each particle, individually. The observations in E&H for two particles side by side falling under gravity show the promising point of applying this formulation to cases wherein multiple particles are in a cell. In the next section, the results of the present correction scheme are discussed and the accuracy of the scheme is assessed.

3. Results

In this section, the present correction scheme is verified by performing several test cases involving unbounded and wallbounded flows. Different flow parameters and grid aspect ratios are carried out in order to assess the robustness of the model for a wide range of applications. In the first set of computations, we start with settling velocity of a particle in an unbounded flow wherein the wall effects do not appear and the model for the collocated arrangements is validated against the analytical solution. In the second set of test cases, the model is validated for velocity of a particle settling parallel and close to a no-slip wall. Test cases at different wall distances, ranging from near to sufficiently away from the wall, are performed to test the model for possible situations that happen in particle-laden flows. Different grid aspect ratios representative of typical turbulent channel flows are used in these tests. In the third set of assessments, the model will be employed to freely falling motion of a particle normal to the wall. The grid resolution for all cases was set to be 128³ as it was found to be sufficient to produce the results that are grid independent.

The three shared non-dimensional flow parameters among cases are those defined based on the Stokes flow in an unbounded configuration. The first one is the Stokes parameter, St, defined as the ratio of the particle relaxation time, τ_{n} , to the fluid time scale, τ_f , as,

$$St = \frac{\tau_p}{\tau_f},\tag{32}$$

where.

$$\tau_p = \frac{\rho_p d_p^2}{18\mu},\tag{33}$$

and,

$$\tau_f = \frac{\min\left(a^{(i)}\right)^2}{v},\tag{34}$$

The second parameter is the particle Reynolds number as,

$$Re_p^{Stk} = \frac{|\mathbf{u}_s^{Stk}|d_p}{V},\tag{35}$$

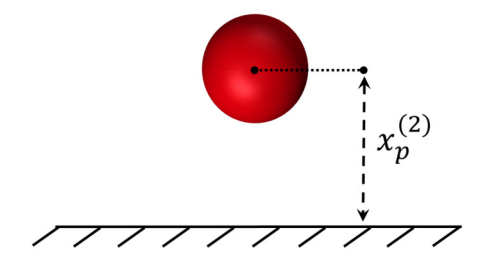


Fig. 5. Particle located at wall distance of $x_p^{(2)}$ near a no-slip wall.

where,

$$\mathbf{u}_{s}^{Stk} = \left(1 - \frac{\rho_{f}}{\rho_{p}}\right) \tau_{p} \mathbf{g},\tag{36}$$

is the particle settling velocity under gravity, **g**, in an unbounded Stokes flow. The third parameter that has three components is the ratio of particle diameter to the grid size as,

$$\Lambda^{(i)} = \frac{d_p}{a^{(i)}}.\tag{37}$$

For wall-bounded test cases, another non-dimensional parameter that is the normalized wall distance from the bottom of the particle is defined as (see Fig. 5),

$$\delta_p = \frac{x_p^{(2)}}{d_p} - 0.5,\tag{38}$$

wherein $x_p^{(2)}$ is the wall distance from the centre of the particle. Concerning complex geometries, computing this distance to the nearest wall might not be straightforward and would have to be investigated in the future. It should be noted that in wall-bounded cases, since the particle drag coefficient changes due to the presence of wall, its actual Reynolds number differs from its unbounded counterpart expressed by Eq. (35).

For the first and second test cases, we evaluate the accuracy of the model based on the errors in the settling, drifting and total velocities of the particle compared to their reference values. Accordingly, the particle velocity, $\mathbf{u}_p(t)$, is decomposed into two components; parallel and perpendicular to the reference velocity of \mathbf{u}_r . The parallel component is expressed as,

$$\mathbf{u}_p^{\parallel} = \frac{\mathbf{u}_r \cdot \mathbf{u}_p(t)}{|\mathbf{u}_r|^2} \mathbf{u}_r,\tag{39}$$

while the perpendicular component is obtained by,

$$\mathbf{u}_p^{\perp} = \mathbf{u}_p(t) - \mathbf{u}_p^{\parallel}. \tag{40}$$

The errors in these two velocity components are then calculated based on the following metrics,

$$e^{\parallel} = \frac{\overline{\mathbf{u}_p^{\parallel}(t).\mathbf{u}_r}}{|\mathbf{u}_r|^2} - 1; \tag{41}$$

$$e^{\perp} = \frac{\overline{|\mathbf{u}_p^{\perp}(t)|}}{|\mathbf{u}_r|},\tag{42}$$

where, overbar $\overline{()}$ denotes the time averaging. Finally, error in the total velocity compared to the reference velocity is obtained as.

$$e = \frac{\overline{|\mathbf{u}_p(t) - \mathbf{u}_r|}}{|\mathbf{u}_r|}.$$
 (43)

The reference velocity, \mathbf{u}_r , is the settling velocity of particle in the gravity direction that is defined differently for each case depending on the corresponding drag coefficient.

Concerning the computations of this part, the numerical method explained in section 2.1 is used here, as well. For each case and at each time step, the fluid velocity at the particle's location, required for the drag force computation, is interpolated using a trilinear function and the nearby fluid control volumes. Given the force balance acting over the particle, it is advanced using a first order Euler approximation. Then, its drag force is applied back to the nearby fluid control volumes using the trilinear function. Knowing these forces added to the fluid phase momentum equation as source terms, the procedure explained in section 2.1 is followed to advance the fluid phase.

Table 2 Listed are the percentage errors for settling, drifting and total velocity of a particle settling in an unbounded domain. Results with and without the present correction scheme are compared with the corresponding values from E&H. Various cases with different particle diameter to grid sizes, Λ , particle Reynolds numbers, Re_p , and particle Stokes numbers, St, are shown for validation.

Case	Re_p^{Stk}	St	$\Lambda^{(1)}$	$\Lambda^{(2)}$	$\Lambda^{(3)}$	uncorrected			E&H			present model		
						e^{\parallel}	e^{\perp}	e	e^{\parallel}	e^{\perp}	e	e^{\parallel}	e^{\perp}	е
U01	0.1	10.0	1.0	1.0	1.0	78.94	0.074	78.94	0.83	0.44	1.00	0.59	0.74	1.05
U02	0.1	10.0	5.0	5.0	5.0	392.14	0.25	392.14	1.70	5.20	7.50	-1.98	7.40	10.97
U03	0.1	10.0	5.0	0.5	0.5	57.40	7.98	57.96	-2.00	1.80	2.90	-3.91	2.07	4.59
U04	0.1	10.0	4.0	2.0	0.2	51.22	10.65	51.32	-3.50	6.00	7.30	-4.62	2.61	5.70
U05	0.5	10.0	1.0	1.0	1.0	68.64	0.08	68.64	4.30	2.00	4.70	4.83	2.29	5.35
U06	0.1	0.25	1.0	1.0	1.0	78.73	0.57	78.73	0.43	0.86	1.40	-0.1	1.86	2.85

3.1. Settling particle in an unbounded flow

In the test cases here, we first validate the present correction scheme for the unbounded regime in order to assess the presented $K_c^{(i)}$ equation as well as the new characteristic length employed for normalization of Eq. (20). Settling velocity of a particle in an unbounded periodic domain is performed. For the results of this part, we neglect the wall effects by setting $\Psi_k^{(i)} = \Phi_{kj}^{(i)} = 1$. For all test cases, a particle that is initially stationary, $u_p^{(i)} = 0$, thus $u_c^{(i)} = 0$, and located in an unbounded flow settles under gravity and in the presence of the stokes drag force. Following the advice by [23], gravity vector is chosen as $\mathbf{g} = (1, (1 + \sqrt{5})/2, \exp(1))/|\mathbf{g}|$ so that particle sweeps through different locations among its adjacent computational cells ensuring that the model is capable of handling any arbitrary positioning of particle. The particle equation of motion in a quiescent fluid is then written as,

$$\frac{d\mathbf{u}_p}{dt} = \left(1 - \frac{\rho_f}{\rho_p}\right)\mathbf{g} - \frac{f}{\tau_p}\mathbf{u}_p,\tag{44}$$

where *f* corresponds to any adjustment factor to the Stokes drag coefficient, which is unity for the studied cases in this part. Accordingly, the analytical solution for the particle velocity for Stokes flow is obtained as,

$$\mathbf{u}^{Stk}(t) = \mathbf{u}_s^{Stk} \left(1 - \exp(-\frac{t}{\tau_p}) \right),\tag{45}$$

where \mathbf{u}_s^{Stk} is the settling velocity provided by Eq. (36) and serves as the reference velocity. Table 2 shows six different cases with various flow parameters and grid aspect ratios for all which the error in settling velocity of the particle without the correction is remarkably large. Errors in settling, drifting and total velocities of the particle predicted with and without the present correction scheme are compared. Additionally, the corresponding values from E&H are listed for comparison. It is worth mentioning that the time step used for the computations of the current cases is half of those reported in [23] so that the Peclet number of $Pe=6\nu\Delta t/min(a^{(i)})^2=0.18$ as well as particle Courant number of $CFL_n=\Delta t/\tau_n=0.003$ are satisfied.

In general, the present scheme reduces the errors with the same order of magnitude as E&H. The slight difference between the results of these two schemes is attributed to the different computation of K_p and K_c . For the low aspect ratio cases (U01-06 except U04), since the present K_c formulation and that of E&H produce almost identical predictions (see Fig. 2 for $K_c < 1$), therefore the embedded error in the collocated grid arrangement, used in this study, yields larger errors in the computation of α_{kj} , K_p and consequently particle settling velocity. For larger aspect ratio case (U04), however, the present K_c expression results in better estimations and compensates the collocated grid arrangement error with better predictions for particle settling velocity. Fig. 6 shows the particle velocity of case U01 as a function of time with and without the correction scheme. As illustrated, the present correction scheme produces excellent result compared to the reference velocity.

3.2. Settling particle parallel to the wall

As the first step toward validating wall effects in the present correction scheme, velocity of a particle settling parallel to a no-slip wall is tested at different wall distances. In order to illustrate the need for the present scheme, results with and without accounting for $\Psi_k^{(i)}$ and $\Phi_{kj}^{(i)}$ (wall effects) in the formulation are compared against the reference. As listed in Table 3, different flow parameters, grid aspect ratios and particle to grid sizes are carried out to assess the capability of the model for a wide range of applications. For the studied cases, a particle that is initially located at a normalized wall gap, δ_p , released to reach its settling velocity under a gravity vector of $\mathbf{g}=(\exp(1),0,(1+\sqrt{5})/2)/|\mathbf{g}|$ that guarantees the particle's motion on a plane parallel to the wall. In reality, the particle experiences a lateral force [51,52], yet in this study other directions are neglected in order to isolate the parallel motion. The particle's equation of motion in the presence of wall follows Eq. (44) with the correction factor of f that is employed based on the work of [44]. In their work, an empirical drag coefficient is derived as a function of normalized wall gap, δ_p , and the relative Reynolds number, Re_p , for a spherical object moving parallel to the wall and in a quiescent flow as,

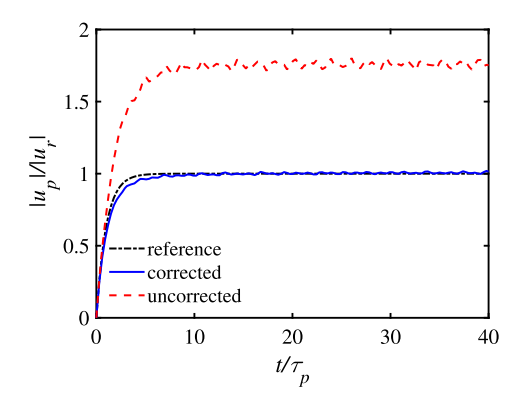


Fig. 6. Plotted is the velocity of a settling particle as a function of time in an unbounded domain. Analytical solution (dash-dotted black), prediction of the present correction scheme (solid blue) as well as the uncorrected scheme (dashed red) are compared. The reference velocity, u_r , used for normalization is the particle settling velocity in Stokes flow given by Eq. (36). Results pertain to case U01 from Table 2. (For interpretation of the colours in the figure(s), the reader is referred to the web version of this article.)

$$C_d^{w,||} = \frac{24}{Re_p} f^{||}(\delta_p, Re_p),$$
 (46)

where $f^{\parallel}(\delta_p, Re_p)$ is the correction factor to the Stokes drag including two terms as,

$$f^{||}(\delta_{p}, Re_{p}) = f_{1}^{||}(\delta_{p}) f_{2}^{||}(\delta_{p}, Re_{p}), \tag{47}$$

where,

$$f_1^{||}(\delta_p) = \left[1.028 - \frac{0.07}{1 + 4\delta_p^2} - \frac{8}{15} \log \left(\frac{270\delta_p}{135 + 256\delta_p} \right) \right]; \tag{48}$$

$$f_2^{||}(\delta_p, Re_p) = \left[1 + 0.15\left(1 - \exp\left(-\sqrt{\delta_p}\right)\right) Re_p^{\left(0.687 + 0.313 \exp\left(-2\sqrt{\delta_p}\right)\right)}\right]. \tag{49}$$

 $f_1^{||}(\delta_p)$ captures the wall effects on the Stokes drag for zero Re_p which becomes unity for large δ_p , recovering the Stokes drag coefficient. $f_2^{||}(\delta_p,Re_p)$, however, handles the wall-modified finite Reynolds number effects to the Stokes drag that converts to the standard Schiller-Naumman correction factor [49] when particle travels sufficiently away from the wall.

For the first cases studied in this part, Re_p is very small, thus only $f_1^{||}(\delta_p)$ holds. The reference for particle velocity is then directly solved as,

$$\mathbf{u}^{w,||}(t) = \mathbf{u}_s^{w,||} \left(1 - \exp\left(-\frac{t}{\tau_p} f_1^{||}(\delta_p) \right) \right), \tag{50}$$

where, $\mathbf{u}_{s}^{w,||}$ is the particle settling velocity in parallel motion to the wall and in the limit of $Re_{p}\sim0$ as,

$$\mathbf{u}_{s}^{w,||} = \left(1 - \frac{\rho_{f}}{\rho_{p}}\right) \frac{\tau_{p}\mathbf{g}}{f_{1}^{||}(\delta_{p})}.$$
(51)

Based on this drag formulation, the actual particle relaxation time in the presence of wall then becomes,

$$\tau_p^{w,||} = \frac{\tau_p}{f_1^{||}(\delta_p)}.\tag{52}$$

Results based on the prediction of different schemes are compared with the reference given by Eq. (50). Following the metrics presented in the preceding section, the errors in settling, drifting and total velocities are measured and compared among different schemes. Table 3 shows these errors for the studied cases of this part which includes five sets, each of which has six cases corresponding to settling at different normalized wall gaps. Results with and without the wall correction factors on the correction scheme, $\Psi_k^{(i)}$ and $\Phi_{kj}^{(i)}$, are compared together with those of the uncorrected scheme to quantify the need for the wall-modified correction scheme. For all studied cases, the particle Reynolds number of Re_p^{Stk} =0.1 and Stokes number of St=10, that are based on unbounded parameters, are kept constant. In practice, however, the actual particle Reynolds number decreases when it gets closer to the wall owing to the larger drag, which is studied separately in the next part.

Sets A and B correspond to isotropic grid configuration with two different particle diameter to grid sizes, whereas the rest, C-F, pertain to anisotropic grids with various aspect ratios. The grid resolution used in the latter are those commonly

Table 3Tabulated are the percentage errors in the simulated velocity of a single particle settling parallel to a wall under gravity and at different normalized wall gaps. Different sets of computations including various types of grid aspect ratio as well as particle diameter to the grid size, $\Lambda^{(i)}$ are studied. For each set, different wall gaps of δ_p are examined to study the error in the settling velocity, e^{\parallel} , drifting velocity, e^{\perp} , and the overall error, e. Flow parameters are kept constant in all cases with Stokes number of St=10 and unbounded particle Reynolds number of $Re_p^{Stk}=0.1$. The results of the wall-modified version of the correction scheme are compared with its unbounded counterpart as well as the classical uncorrected point-particle approach.

Case	δ_p	$\Lambda^{(1)}$	$\Lambda^{(2)}$	$\Lambda^{(3)}$	uncorrect	ed		corrected unbounde			corrected using wall-modified version		
					e^{\parallel}	e^{\perp}	e	e^{\parallel}	e^{\perp}	e	e^{\parallel}	e^{\perp}	е
A1	0.05	1.0	1.0	1.0	125.82	0.17	125.82	-86.82	21.42	91.42	5.37	2.23	6.03
A2	0.5	1.0	1.0	1.0	59.16	0.095	59.16	-35.08	1.37	35.12	4.86	0.57	4.91
A3	1.0	1.0	1.0	1.0	103.12	0.073	103.12	-19.67	1.16	19.72	4.29	0.76	4.38
A4	1.5	1.0	1.0	1.0	66.12	0.073	66.12	-13.81	0.66	13.84	4.06	0.46	4.10
A5	2.0	1.0	1.0	1.0	102.96	0.06	102.96	-10.02	0.87	10.08	2.08	0.72	2.24
A6	∞	1.0	1.0	1.0	69.19	0.05	69.19	0.74	0.45	0.95	1.0	0.44	1.14
B1	0.05	5.0	5.0	5.0	745.72	0.54	745.72	-102.6	142.86	212.04	-3.02	13.66	19.50
B2	0.5	5.0	5.0	5.0	437.08	0.28	437.08	-31.02	20.99	42.67	4.51	6.96	11.16
В3	1.0	5.0	5.0	5.0	589.81	0.16	589.8	-22.48	10.12	28.80	-4.17	9.77	17.54
B4	1.5	5.0	5.0	5.0	390.42	0.22	390.42	-10.43	6.02	15.35	4.78	5.58	10.01
B5	2.0	5.0	5.0	5.0	554.19	0.15	554.19	-9.99	8.89	20.14	-0.59	9.08	16.06
B6	∞	5.0	5.0	5.0	353.79	0.2	353.79	0.35	5.01	9.16	0.83	4.85	8.97
C1	0.05	0.1	1.0	0.2	7.91	0.17	7.91	-33.79	2.12	33.87	0.58	0.33	0.67
C2	0.5	0.1	1.0	0.2	5.59	0.25	5.59	-18.12	1.14	18.16	1.03	0.32	1.08
C3	1.0	0.1	1.0	0.2	9.82	0.46	9.83	-11.47	0.78	11.51	1.29	0.53	1.40
C4	1.5	0.1	1.0	0.2	8.93	0.58	8.95	-11.27	0.62	11.29	0.71	0.59	0.93
C5	2.0	0.1	1.0	0.2	11.98	0.77	12.01	-7.55	0.42	7.57	0.55	0.65	0.86
C6	∞	0.1	1.0	0.2	14.88	1.09	14.92	-2.16	0.25	2.19	-1.89	0.25	1.92
D1	0.05	0.5	5.0	1.0	106.87	7.99	107.17	-69.94	3.33	70.02	-3.04	7.25	8.40
D2	0.5	0.5	5.0	1.0	82.44	7.69	82.80	-44.12	1.03	44.15	-12.55	4.7	13.45
D3	1.0	0.5	5.0	1.0	95.70	8.00	96.04	-16.49	1.93	16.64	-4.21	2.72	5.05
D4	1.5	0.5	5.0	1.0	82.49	7.24	82.81	-20.79	1.17	20.84	-9.87	2.14	10.23
D5	2.0	0.5	5.0	1.0	94.04	7.12	94.31	-9.59	0.84	9.64	-0.78	1.58	3.13
D6	∞	0.5	5.0	1.0	79.99	5.95	80.21	-10.84	1.01	10.92	-9.53	0.99	9.63
E1	0.05	0.3	6.0	0.6	42.99	2.14	43.05	-43.24	2.93	43.34	-0.69	1.54	1.71
E2	0.5	0.3	6.0	0.6	50.17	3.78	50.31	-21.67	0.9	21.69	-3.15	1.34	3.45
E3	1.0	0.3	6.0	0.6	49.20	4.28	49.39	-16.29	0.14	16.29	-4.33	1.40	4.58
E4	1.5	0.3	6.0	0.6	48.27	4.34	48.47	-12.23	0.91	12.28	-4.43	1.77	4.88
E5	2.0	0.3	6.0	0.6	56.16	5.08	56.39	-9.27	0.65	9.29	-3.47	1.2	3.68
E6	∞	0.3	6.0	0.6	53.61	4.05	53.77	-5.47	0.23	5.48	-4.41	0.31	4.42
F1	0.05	0.6	12.0	1.2	113.56	8.25	113.86	-50.01	1.61	50.03	-4.82	4.09	6.52
F2	0.5	0.6	12.0	1.2	121.47	11.00	121.97	-19.90	1.18	19.94	-3.06	3.01	4.44
F3	1.0	0.6	12.0	1.2	113.10	9.81	113.53	-12.64	1.51	12.74	-3.03	2.47	4.2
F4	1.5	0.6	12.0	1.2	108.30	8.8	108.66	-10.05	1.25	10.13	-3.48	1.86	4.27
F5	2.0	0.6	12.0	1.2	105.95	8.24	106.27	-8.19	1.01	8.26	-3.28	1.44	3.82
F6	∞	0.6	12.0	1.2	100.45	7.42	100.72	-6.05	0.72	6.10	-4.12	0.90	4.27

encountered in the turbulent channel flows. The first observation from Table 3 is that the errors for the uncorrected scheme are significantly large for all cases, necessitating the need for correcting the Point-Particle approach even in the presence of a no-slip wall. In addition, consistent with observation of E&H, the error in uncorrected results increases proportional to $(\Lambda^{(1)}\Lambda^{(2)}\Lambda^{(3)})^{1/3} \propto d_p/d_c$. As an example, the error in total velocity of the uncorrected scheme for case C1 is two order of magnitude smaller than that of case B1 wherein the volume ratio of particle to the grid is much greater.

In the first place, one could correct the PP results with the unbounded version of the present correction scheme wherein wall effects are ignored, i.e., $\Psi_k^{(i)} = \Phi_{kj}^{(i)} = 1$. As listed in Table 3, for wall distances very close to the wall, such as $\delta_p = 0.05$ and 0.5, the unbounded version under predicts the particle velocity with negative errors on the same order of magnitude as the uncorrected scheme. The large error in the results of the near wall region is due to the overprediction in the disturbance velocity of the unbounded correction scheme, while particle in practice receives much smaller \mathbf{u}_c from the background flow in that region. When particle gets away from the wall, however, the predicted disturbance field using unbounded version becomes more accurate and reduces the errors significantly (see cases at $\delta_p = \infty$).

When wall effects are accounted for in the correction scheme, i.e., $\Psi_k^{(i)} \neq 1$ and $\Phi_{kj}^{(i)} \neq 1$, the asymmetry pattern is captured with producing much better predictions. For the cases considered, the errors reduce to one order of magnitude smaller values when the wall-modified correction scheme is applied. For example, in case A1, the total error of 91.42% in particle settling velocity predicted by the unbounded correction scheme reduces to 6.03% when wall effects are accounted for. Additionally, for particles travelling far away from the wall wherein the symmetric disturbance field is expected, the wall-

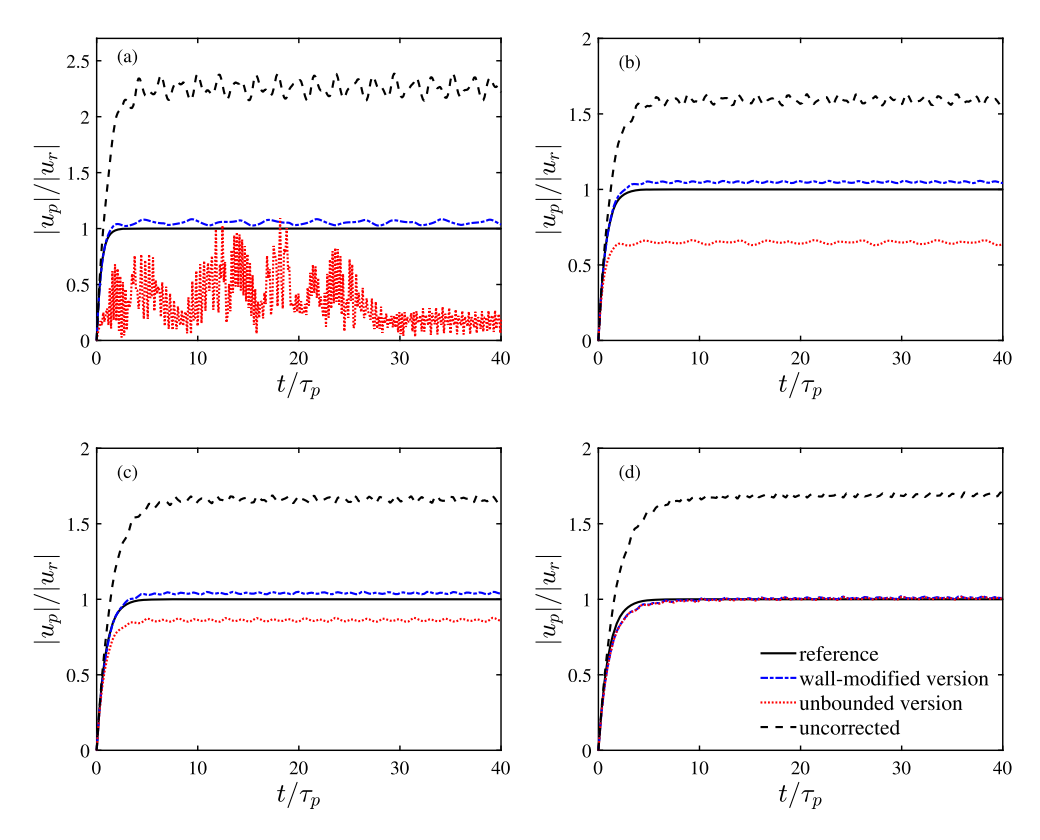


Fig. 7. Shown are velocity of a particle settling under gravity parallel to a wall at different wall distances of (a): δ_p =0.05, (b): δ_p =0.5, (c): δ_p =1.5 and (d): δ_p =∞. Results of the present scheme with wall-modified version (dash-dotted blue), unbounded version (dotted red) and uncorrected scheme (dashed black) are all compared against the reference velocity (solid black). These results are based on case A of Table 3.

modified and unbounded versions of the present correction scheme both yield nearly identical results. It should be noted that the inconsiderable difference between these two versions at $\delta_p = \infty$ is attributed to the approximation of Φ_{kj} and Ψ_k and their slight deviation from unity for this wall distance.

Fig. 7 illustrates the results of these two versions on the particle velocity of case A as a function of time. The improvement in the results of the wall-modified version shows its potential superiority to the unbounded version for wall-bounded particle-laden flows. In a parallel study, [32] show similar observations that accounting for wall effects in the correction scheme increases greatly the accuracy of the particle velocity in the case of settling parallel to a wall.

The results presented in the previous part were obtained for $Re_p < 0.1$, while in the wall-bounded particle-laden flows, typically a wider range of Re_p exists. In this part, the present model is tested for a range of Re_p up to 10 by performing similar computations to the previous part. Table 4 lists the studied cases for this part that are similar to case E1 of Table 3, yet with different Stokes and particle Reynolds numbers. Unlike the previous part, the reported particle Reynolds number here is based on its actual velocity and defined by $Re_p = Re_p^{Stk}/f^{||}(\delta_p, Re_p)$ which varies from 0.044 to 10. For all cases, settling is performed at $\delta_p = 0.05$ for which the deviation between the unbounded and wall-modified versions of the correction scheme was found to be significant. For studied cases here, the whole terms in Eq. (47) hold, and we use the result of the one-way coupled simulation as the reference since the background flow remains undisturbed.

As shown in Table 4, the error in uncorrected scheme is reduced as Re_p increases which is in line with the observations of the preceding works [24,28]. This can be justified that higher Reynolds number particles move faster and their residency time in their own disturbance field created in the previous time step is smaller than that of the slower particles, hence less disturbance. In addition, [28] showed that as Re_p increases, the region of maximum disturbance travels farther downstream so that \mathbf{u}_c sampled at the particle location will be smaller for larger Re_p . Hence, the finite Reynolds number effect is not solely due to increased speed from one time step to the next, but also the relative importance of particle motion to viscous diffusion of the disturbance field, which can be important even if the particle does not move. Although this diminishes the need for the correction for large Re_p , the error of approximately 30% that pertains to the case with Re_p =10 (the largest studied Re_p), is still considerable. As listed in Table 4, the wall-modified version of the correction scheme reduces the errors by approximately one order of magnitude for cases with Re_p <10 and results in better predictions compared to the unbounded version.

It should be emphasized that the present model is constructed based on the small Re_p assumption. Although the finite Re_p effects are partially accounted for through the correction factor of C_r (Eq. (29)), a more elaborate formulation is required

Table 4The effects of particle Reynolds number, Re_p , and particle Stokes number, St, on the velocity of a single particle settling parallel and close to a wall at δ_p =0.05 are shown. The anisotropic grid resolution of case E from Table 3 with Λ =[0.3, 6.0, 0.6] is employed for all cases. The wall-modified and unbounded versions of the present correction scheme are compared together and against the uncorrected PP approach in terms of the error in settling velocity, e^{\parallel} , drifting velocity, e^{\perp} and total velocity, e.

Case Rep	Re_p	St	uncorrected			corrected unbounded	0		corrected using wall-modified version		
			e	e^{\perp}	е	e^{\parallel}	e^{\perp}	е	e^{\parallel}	e^{\perp}	e
R1	0.044	3.0	32.94	1.64	32.99	-41.59	2.77	41.68	-3.10	0.77	3.20
R2	0.044	10.0	40.80	2.02	40.85	-41.58	2.84	41.68	-2.74	0.86	2.88
R3	0.044	30.0	61.31	3.09	61.38	-47.91	3.63	48.05	-6.75	1.23	6.87
R4	0.5	3.0	50.95	2.60	51.02	-48.35	3.99	48.52	-4.11	1.43	4.66
R5	0.5	10.0	53.11	2.68	53.18	-49.24	3.74	49.41	-1.86	1.31	2.78
R6	0.5	30.0	52.43	2.62	52.50	-47.14	3.07	47.26	-1.46	1.24	2.11
R7	5.0	3.0	39.62	1.77	39.66	-26.45	2.34	26.58	2.76	1.11	3.18
R8	5.0	10.0	39.77	1.76	39.81	-26.18	2.40	26.31	2.96	1.10	3.23
R9	5.0	30.0	39.90	1.76	39.94	-26.16	2.37	26.27	3.04	1.10	3.24
R10	10.0	3.0	33.56	1.26	33.59	-17.60	2.23	17.77	5.25	0.76	5.31
R11	10.0	10.0	34.06	1.27	34.09	-17.45	2.26	17.60	5.45	0.76	5.50
R12	10.0	30.0	33.92	1.26	33.94	-17.39	2.27	17.54	5.40	0.74	5.45

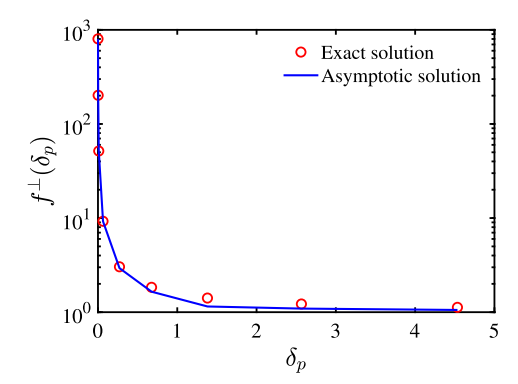


Fig. 8. Shown is the wall adjustment to the drag coefficient of a particle in wall-normal motion. Exact solution of [42] is shown along with the asymptotic solution provided by [42] and [53], given in Eq. (53).

to improve the accuracy of the model for $Re_p > 10$. For such cases, the assumption of symmetric Stokes solution is not valid anymore and the linear superposition of the perturbations caused by neighbour cells used in the derivation of K_p may be broken. Such adjustments for $Re_p > 10$ are left for future investigations. Concerning the Stokes number effect, our results show insignificant changes to the prediction of the present model for the studied range of 3 < St < 30.

3.3. Free falling particle normal to the wall

This section verifies the present model for capturing the disturbance field in the wall-normal motion of particles, as commonly encountered in wall-bounded particle-laden flows. The free falling motion of a particle normal to the wall is considered as a test case for this part. In such scenario, as particle falls under gravity and approaches the wall its drag coefficient increases owing to the wall lubrication effect. [42] derived an exact solution for the wall adjustment to the drag coefficient of a particle in wall normal motion with small Reynolds number of $Re_p < 0.1$. In their work, a corresponding asymptotic solution was also obtained that matches their exact solution for the normalized wall gaps of $\delta_p > 1.38$. For $\delta_p < 1.38$, [53] achieved an asymptotic solution that combined with the asymptotic one obtained by [42], are used in this work for the wall adjustment to the drag coefficient of a particle in wall-normal motion. This adjustment is expressed as,

$$f^{\perp}(\delta_p) = \begin{cases} 1 + \left(\frac{0.562}{1+2\delta_p}\right) & \text{for } \delta_p > 1.38 \quad [42] \\ \frac{1}{2\delta_p} \left(1 + 0.4\delta_p \log\left(\frac{1}{2\delta_p}\right) + 1.94\delta_p\right) & \text{for } \delta_p < 1.38 \quad [53]. \end{cases}$$
(53)

Fig. 8 compares these asymptotic solutions to the exact solution of [42]. The reference case for this part is obtained based on the one-way coupled simulation wherein the background flow is not disturbed by the particle. For all the studied cases, the particle is initially stationary and located at the normalized wall gap of δ_p =7 and falls under gravity. Similar to

Table 5 Percentage errors calculated in the prediction of particle's wall-normal motion. Two sets of grid aspect ratio with various particle Reynolds numbers and Stokes numbers are performed. For each case, the error in the time that particle requires to reach the normalized wall gap of δ_p =0.5 is computed based on the wall-modified and unbounded versions of the present correction scheme in comparison with that of the uncorrected scheme.

Case	Re _p ^{Stk}	St	$\Lambda^{(1)}$	$\Lambda^{(2)}$	$\Lambda^{(3)}$	uncorrected	corrected using unbounded version	corrected using wall-modified version
						e	e	e
N1	0.1	3.0	1.0	1.0	1.0	-30.55	32.30	-6.05
N2	0.1	10.0	1.0	1.0	1.0	-24.37	23.86	-4.77
N3	0.1	30.0	1.0	1.0	1.0	-15.09	10.13	-2.79
N4	5.0	10.0	1.0	1.0	1.0	-2.30	0.97	-0.07
N5	10.0	10.0	1.0	1.0	1.0	-1.37	0.62	0.02
N6	0.1	3.0	0.3	6.0	0.6	-9.62	4.95	-2.88
N7	0.1	10.0	0.3	6.0	0.6	-9.61	5.04	-2.75
N8	0.1	30.0	0.3	6.0	0.6	-9.57	4.78	-2.87
N9	5	10.0	0.3	6.0	0.6	-1.80	0.72	-0.24
N10	10	10.0	0.3	6.0	0.6	-0.73	0.52	0.1

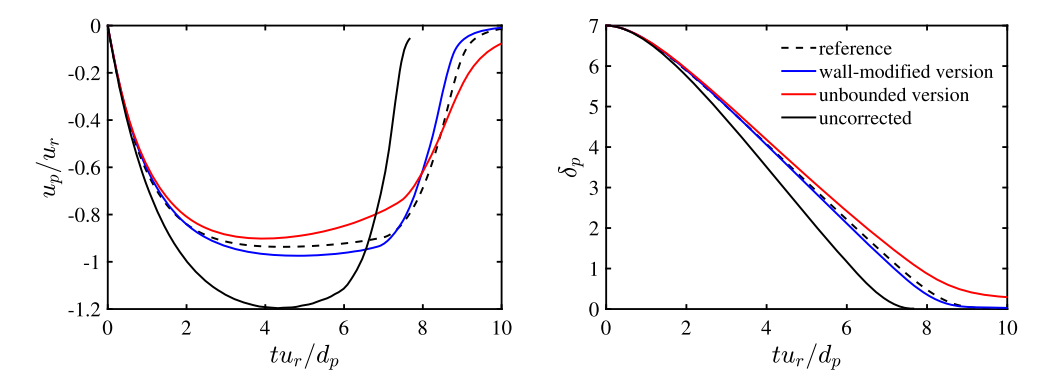


Fig. 9. Shown are the normalized velocity (left) and normalized wall-gap (right) of a particle settling normal to a wall, corrected by the wall-modified and unbounded versions of the present scheme. Results are compared with the uncorrected approach as well as the reference that is based on the one-way coupled simulation. Results here pertain to the case N2 from Table 5.

the preceding section, results of the wall-modified and unbounded versions of the present correction scheme are compared with those of the uncorrected approach. Studied cases are listed in Table 5 that are carried out using both isotropic and anisotropic grids. A range of particle Reynolds number of $0.04 < Re_p < 10$ and Stokes number of 3 < St < 30 are used for each grid resolution. It should be noted that the drag expression provided by Eq. (53) is valid for $Re_p < 0.1$, however, we still use it for larger Re_p cases to show a numerical demonstration of the present scheme without advocating that the chosen drag coefficient is realistic for large Re_p cases. For each case, the total time that particle requires to reach the normalized wall gap of $\delta_p = 0.5$ is computed and compared against the corresponding reference value, t_{ref} , that is obtained based on the one-way coupled simulation. The deviation of each scheme from the reference is quantified based on the following metric,

$$e = \frac{t - t_{ref}}{t_{ref}}. ag{54}$$

As Table 5 shows, without correcting the PP approach, the considerable and negative errors for each case imply the fact that particle sees a smaller drag force due to the disturbance created in the background flow, accelerates faster and reaches the wall-gap of interest quicker. However, when the PP is corrected using the wall-modified version of the correction scheme, it reduces the errors and results in better prediction for the particle trajectory and velocity. Although the errors obtained based on the unbounded version are still better than the uncorrected approach, the superiority of the wall-modified version on other schemes is noticeable here as well.

Fig. 9 shows the prediction of the different schemes on the particle velocity and trajectory of case N2 from Table 5. The velocity that is used for normalizing the parameters of this part (u_r) is based on Eq. (36) that pertains to the Stokes settling velocity of a particle in an unbounded domain. As illustrated, the wall-modified version of the present scheme captures quite well the accurate trajectory and velocity of the particle whereas the unbounded version hinders the particle settling due to the overprediction in the disturbance field. Results in this part along with the observation of the previous parts underscore the importance of the present wall-modified correction scheme for flows with and without no-slip boundaries.

Concerning more sophisticated scenarios such as particle close to two different walls or a corner, we conjecture that in the limit of creeping flow for the disturbance field, $Re_c < 0.1$, a linear superposition of the disturbance created by each wall is possible as a first order estimate. However, we leave the investigations of such scenarios for future works.

4. Conclusion

Modelling two-way coupled Euler-Lagrange (EL) particle-laden flows using point-particle (PP) approach can result in erroneous predictions due to an issue that arises in the calculation of the fluid forces acting on the particles. The available closures for force calculations are based on the undisturbed fluid velocity, which by definition is the fluid velocity not influenced by the presence of particles. In two-way coupled computations, however, the particle reaction force disturbs the fluid velocity around the particle and using such a disturbed velocity for force calculations in the next time step, yields inaccurate inter-phase interactions and wrong predictions. More importantly, depending on whether the particle is travelling near a no-slip boundary or in an unbounded domain, its disturbance in the background flow can be different in terms of shape and strength, and can also be asymmetric.

In this paper, we presented a correction scheme for EL-PP approaches to recover the undisturbed fluid velocity from the available disturbed field in the presence and absence of smooth no-slip walls. In the present approach, the disturbance created by a particle in a computational cell that carries the particle is obtained by finding the response of the cell (its velocity) to the particle force. Analogous to the motion of a solid object, the disturbance velocity of the computational cell is obtained by treating the cell as a solid object that is subjected to the particle force and dragged through the adjacent computational cells [27]. Knowing these two forces, the disturbance velocity of the cell is solved using a first-order ordinary differential equation for the computational cell. The model can be used for (i) unbounded and wall-bounded regimes, (ii) isotropic and anisotropic rectilinear grids, (iii) particles bigger than the grid size, (iv) arbitrary interpolation and projection functions, and (v) flows with finite particle Reynolds number.

An empirical expression was obtained for the drag coefficient of the computational cell $(K_c^{(i)})$ that is applicable for a wide range of grid aspect ratios, typically encountered in the particle-laden turbulent channel flows. The new expression, obtained based on the employed collocated grid arrangement, is a function of the grid aspect ratio. Just as a slowly moving solid particle in a quiescent fluid influences the near field through Stokes solution, the particle force at a computational cell perturbs the surrounding cells. It was shown that for the employed collocated grid arrangement, Stokes solution normalized by the characteristics length of $0.25d_c$ results in accurate predictions for the disturbance field created in the surrounding cells, compared to our numerical measurements.

Wall effects in the model were taken into account through two different factors; (i) $\Psi_k^{(i)}$ and (ii) $\Phi_{kj}^{(i)}$. The first pertains to the wall adjustment to the drag coefficient of the computational cell near a no-slip boundary, analogous to the near wall motion of a solid object. Two components for this parameter were obtained for the disturbances created in parallel and wall-normal directions. For isotropic grid, it was shown that the wall adjustment to the drag coefficient of a solid sphere moving near a no-slip wall, empirically derived by [44], can be an excellent choice for $\Psi_k^{(i)}$. However, for anisotropic grids owing to their large aspect ratios, this expression does not hold, and a new fitted expression was obtained for a wide range of grid aspect ratios. The second parameter, $\Phi_{kj}^{(i)}$, was introduced to capture the wall effect on the Stokes solution of the computational cell. It was shown that perturbation created at neighbouring cells by a computational cell that is exposed to the particle force differs in shape and strength as the cell becomes closer to a no-slip wall. It was argued that one could directly use the wall-modified Stokes solution instead of its unbounded counterpart, however, due to the complexity and expense embedded in the implementation and solution of the wall-modified version, Stokeslet solution was suggested as the second wall adjustment factor. In that regard, we kept the Stokes solution in the formulation, while its wall effect was accounted for by multiplying this solution by the ratio of the wall-bounded to the unbounded Stokeslet solutions, defined as $\Psi_b^{(i)}$. Our results showed that the choice of this ratio yields in good predictions with small errors.

as $\Psi_k^{(i)}$. Our results showed that the choice of this ratio yields in good predictions with small errors. An unbounded version of the present model can be obtained by letting $\Psi_k^{(i)} = \Phi_{kj}^{(i)} = 1$ in the formulation, that can be used in particle-laden flows without no-slip walls. To verify the collocated adjustments made in the formulation, the unbounded version of the scheme was first tested for settling of a particle in an unbounded domain and results were compared with those reported in [27]. For the different studied flow and grid parameters, it was shown that the model using the collocated grid arrangement accurately captures the settling velocity of the particle with a few percent errors.

To assess the model for wall-bounded applications, settling of a particle parallel to a no-slip wall was performed at various wall-normal distances. Consistent with the observation of [27], the error in the uncorrected particle velocity was observed to be a function of particle's diameter to the grid size, (d_p/d_c) . Correcting the PP approach with the current model, however, captured the disturbance field at all wall distances and significantly reduced the errors in the prediction of particle velocity. Furthermore, it was observed that ignoring the wall effects in the formulation for wall-bounded flows, i.e., assuming $\Psi_k^{(i)} = \Phi_{kj}^{(i)} = 1$, results in large errors that are on the same order of magnitude of the uncorrected scheme, particularly for the near wall motions. As particle gets away from the wall, however, the effects of wall diminish and the formulation approaches the unbounded version.

Tests performed for a range of $0 < Re_p < 10$ revealed the fact that the error in the uncorrected settling velocity decreases as Re_p increases, consistent with the observation of [28]. Nevertheless, the relatively small errors associated with large Re_p cases were still lowered using the present correction scheme.

The last test cases were carried out on the free falling motion of a particle in the wall-normal direction. It was shown that the particle's velocity in the uncorrected scheme is erroneously overpredicted which makes the particle hit the wall earlier than it would in reality. When the PP approach is corrected with the present model, however, it recovers the undisturbed velocity at any wall distance and captures the particle's velocity and trajectory more accurately. Tests performed for this part with different grid configurations and flow parameters showed the superiority of the present model to the uncorrected and unbounded correction schemes.

The present correction scheme is cost-efficient and accurate that can be easily implemented in EL-PP packages to study a wide range of particulate flows with and without the no-slip boundaries. We conjecture that this scheme could help improve the investigations and the state-of-the-art of the wall-bounded particle-laden flows wherein the lack of accuracy of the standard uncorrected PP approaches has been widely observed.

5. Acknowledgements

Financial support was provided under the NASA Contract Number NNX16AB07A monitored by program manager Dr. Jeff Moder, NASA Glenn Research Center as well as The National Science Foundation (NSF) under Grant Numbers 1133363 and 1851389. In addition, the authors acknowledge the San Diego Supercomputer Center (SDSC) at University of California San Diego for providing HPC resources that have contributed to the results reported here.

Declaration of competing interest

The authors declare that they have no known competing financial interests or personal relationships that could have appeared to influence the work reported in this paper.

Appendix A. A simplified equation for $\Psi_{\nu}^{(i)}$ on isotropic grids

A simplified expression for $\Psi_k^{(i)}$ that is only applicable for isotropic rectilinear grids is introduced here. The new equation denoted by Ψ_k^{iso} is obtained based on the work of [44]. In their work, an expression using fully resolved direct numerical simulation was empirically derived for the wall adjustment to the drag coefficient of a solid sphere in parallel motion to a no-slip wall. Our results show that their expression matches our corresponding measured values for isotropic computational cells. Accordingly, the new expression for $\Psi_k^{(i)}$ on isotropic grids is introduced as,

$$\Psi_k^{iso} = \left(1.028 - \frac{0.07}{1 + 4\delta_k^2} - \frac{8}{15}\log\left(\frac{270\delta_k}{135 + 256\delta_k}\right)\right),\tag{55}$$

where

$$\delta_k = \frac{x_k^{(2)}}{0.5d_c} - 0.5,\tag{56}$$

and $x_k^{(2)}$ is the wall-normal distance of the centre of the computational cell k, normalized by its equivalent radius of $0.5d_c$. The choice of these two parameters ($x_k^{(2)}$ and $0.5d_c$) are slightly changed compared to the original formulation of [44], in order to produce better predictions. It is also imperative to mention that Eq. (55) covers a wide range of wall distances and approaches unity when the computational cell is sufficiently away from the wall. Fig. 10 shows the predictions of this equation for both parallel and normal forces compared to the measured values. It should be emphasized that unlike the predictive capability of the equation above for the isotropic grid resolutions, it deviates for highly skewed anisotropic grids.

Appendix B. Stokeslet solutions

In this Appendix, the wall-bounded and unbounded Stokeslet solutions used in the derivation of $\Phi_{kj}^{(i)}$ in section 2, are explained in detail. The unbounded Stokeslet solution that is the flow generated by a point force in an unbounded quiescent fluid with dynamic viscosity of μ is expressed as [48],

$$u_{stkl,un}^{(i)} = \frac{F^{(j)}}{8\pi \mu} \left(\frac{\delta_{ij}}{|r_{kj}|} + \frac{r_{kj}^{(i)} r_{kj}^{(j)}}{|r_{kj}|^3} \right), \tag{57}$$

where,

$$r_{kj}^{(i)} = (x_j^{(i)} - x_k^{(i)}); \quad |r_{kj}| = \sqrt{\sum_{i=1}^{3} (r_{kj}^{(i)})^2}, \tag{58}$$

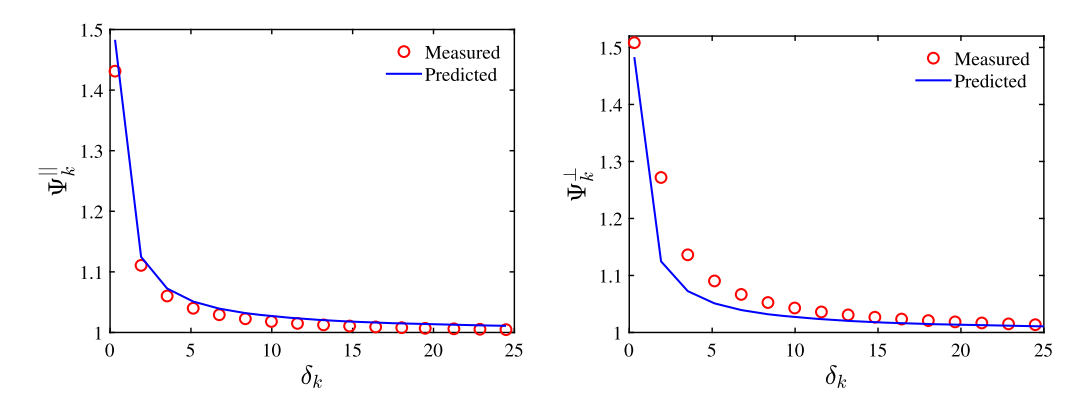


Fig. 10. Shown are the predictions of Eq. (55) for the wall adjustment to the drag coefficient of an isotropic grid compared to the measured values for parallel (left) and perpendicular (right) forces.

and $u^{(i)}$ is the i component of velocity created at the location of $(x_j^{(1)}, x_j^{(2)}, x_j^{(3)})$ by the point force, $F^{(j)}$, exerted in j direction and located at $(x_k^{(1)}, x_k^{(2)}, x_k^{(3)})$. δ_{ij} is the Kronecker delta which is unity for i=j and zero otherwise. Similar to this, the wall-bounded Stokeslet solution for a point force that is applied near a no-slip wall is expressed as [48],

$$u_{stkl,b}^{(i)} = \frac{F^{(j)}}{8\pi \mu} \left[\left(\frac{\delta_{ij}}{|r_{kj}|} + \frac{r_{kj}^{(i)} r_{kj}^{(j)}}{|r_{kj}|^{3}} \right) - \left(\frac{\delta_{ij}}{|R_{kj}|} + \frac{R_{kj}^{(i)} R_{kj}^{(j)}}{|R_{kj}|^{3}} \right) + 2x_{k}^{(2)} \left(\delta_{jm} \delta_{ml} - \delta_{j3} \delta_{3l} \right) \frac{\partial}{\partial R_{kj}^{(l)}} \left(\frac{x_{k}^{(2)} R_{kj}^{(i)}}{|R_{kj}|^{3}} - \left(\frac{\delta_{i3}}{|R_{kj}|} + \frac{R_{kj}^{(i)} R_{kj}^{(2)}}{|R_{kj}|^{3}} \right) \right) \right],$$

$$(59)$$

where,

$$R_{kj}^{(i)} = \begin{cases} r_{kj}^{(i)}, & i = 1, 3\\ r_{kj}^{(2)} + 2x_k^{(2)}, & i = 2 \end{cases}; \quad |R_{kj}| = \sqrt{\sum_{i=1}^{3} (R_{kj}^{(i)})^2}, \tag{60}$$

and $x_k^{(2)}$ is the wall distance at which the force is applied. The rest of parameters are similar to those of the unbounded Stokeslet solution.

References

- [1] D. Mukherjee, J. Padilla, S.C. Shadden, Numerical investigation of fluid-particle interactions for embolic stroke, Theor. Comput. Fluid Dyn. 30 (1–2) (2016) 23–39.
- [2] K. Müller, D.A. Fedosov, G. Gompper, Understanding particle margination in blood flow–a step toward optimized drug delivery systems, Med. Eng. Phys. 38 (1) (2016) 2–10.
- [3] S. Apte, M. Gorokhovski, P. Moin, Les of atomizing spray with stochastic modeling of secondary breakup, Int. J. Multiph. Flow 29 (9) (2003) 1503–1522.
- [4] H. Pouransari, A. Mani, Effects of preferential concentration on heat transfer in particle-based solar receivers, J. Sol. Energy Eng. 139 (2) (2017) 021008.
- [5] X. He, S. Karra, P. Pakseresht, S. Apte, S. Elghobashi, Effect of heated-air blanket on the dispersion of squames in an operating room, Int. J. Numer. Methods Biomed. Eng. 34 (5) (2018) e2960.
- [6] J.R. Finn, M. Li, S.V. Apte, Particle based modelling and simulation of natural sand dynamics in the wave bottom boundary layer, J. Fluid Mech. 796 (2016) 340–385.
- [7] M.R. Maxey, J.J. Riley, Equation of motion for a small rigid sphere in a nonuniform flow, Phys. Fluids 26 (4) (1983) 883-889.
- [8] M. Maxey, B. Patel, E. Chang, L.-P. Wang, Simulations of dispersed turbulent multiphase flow, Fluid Dyn. Res. 20 (1-6) (1997) 143-156.
- [9] S. Elghobashi, Particle-laden turbulent flows: direct simulation and closure models, Appl. Sci. Res. 48 (3-4) (1991) 301-314.
- [10] K.D. Squires, J.K. Eaton, Particle response and turbulence modification in isotropic turbulence, Phys. Fluids A, Fluid Dyn. 2 (7) (1990) 1191-1203.
- [11] S. Elghobashi, G. Truesdell, On the two-way interaction between homogeneous turbulence and dispersed solid particles. I: Turbulence modification, Phys. Fluids A, Fluid Dyn. 5 (7) (1993) 1790–1801.
- [12] J.C. Segura, Predictive capabilities of particle-laden large eddy, simulation, 2005.
- [13] J.K. Eaton, Two-way coupled turbulence simulations of gas-particle flows using point-particle tracking, Int. J. Multiph. Flow 35 (9) (2009) 792-800.
- [14] P. Pakseresht, S.V. Apte, J.R. Finn, On the predictive capability of dns-dem applied to suspended sediment-turbulence interactions, in: ASME 2017 Fluids Engineering Division Summer Meeting, American Society of Mechanical Engineers, 2017, V01BT11A025–V01BT11A025.
- [15] Y. Pan, S. Banerjee, Numerical simulation of particle interactions with wall turbulence, Phys. Fluids 8 (10) (1996) 2733-2755.
- [16] A. Ferrante, S. Elghobashi, On the physical mechanisms of drag reduction in a spatially developing turbulent boundary layer laden with microbubbles, J. Fluid Mech. 503 (2004) 345–355.
- [17] S. Apte, K. Mahesh, T. Lundgren, Accounting for finite-size effects in simulations of disperse particle-laden flows, Int. J. Multiph. Flow 34 (3) (2008) 260–271.
- [18] A.J. Cihonski, J.R. Finn, S.V. Apte, Volume displacement effects during bubble entrainment in a travelling vortex ring, J. Fluid Mech. 721 (2013) 225-267.
- [19] P. Pakseresht, S.V. Apte, Volumetric displacement effects in Euler-Lagrange les of particle-laden jet flows, Int. J. Multiph. Flow 113 (2019) 16–32.

- [20] M. Maxey, B. Patel, Localized force representations for particles sedimenting in Stokes flow, Int. J. Multiph. Flow 27 (9) (2001) 1603-1626.
- [21] S. Lomholt, B. Stenum, M. Maxey, Experimental verification of the force coupling method for particulate flows, Int. J. Multiph. Flow 28 (2) (2002) 225–246
- [22] P. Gualtieri, F. Picano, G. Sardina, C.M. Casciola, Exact regularized point particle method for multiphase flows in the two-way coupling regime, J. Fluid Mech. 773 (2015) 520–561.
- [23] J. Horwitz, A. Mani, Accurate calculation of Stokes drag for point-particle tracking in two-way coupled flows, J. Comput. Phys. 318 (2016) 85-109.
- [24] J. Horwitz, A. Mani, Correction scheme for point-particle models applied to a nonlinear drag law in simulations of particle-fluid interaction, Int. J. Multiph. Flow 101 (2018) 74–84.
- [25] M. Mehrabadi, J. Horwitz, S. Subramaniam, A. Mani, A direct comparison of particle-resolved and point-particle methods in decaying turbulence, J. Fluid Mech. 850 (2018) 336–369.
- [26] P.J. Ireland, O. Desjardins, Improving particle drag predictions in Euler–Lagrange simulations with two-way coupling, J. Comput. Phys. 338 (2017) 405–430
- [27] M. Esmaily, J. Horwitz, A correction scheme for two-way coupled point-particle simulations on anisotropic grids, J. Comput. Phys. 375 (2018) 960-982.
- [28] S. Balachandar, K. Liu, M. Lakhote, Self-induced velocity correction for improved drag estimation in Euler–Lagrange point-particle simulations, J. Comput. Phys. 376 (2019) 160–185.
- [29] K. Liu, M. Lakhote, S. Balachandar, Self-induced temperature correction for inter-phase heat transfer in Euler-Lagrange point-particle simulation, J. Comput. Phys. 396 (2019) 596–615.
- [30] P. Pakseresht, M. Esmaily, S.V. Apte, A correction scheme for two-way coupled Euler-Lagrange wall-bounded flows, Bull. Am. Phys. Soc. (2019).
- [31] J. Horwitz, G. Iaccarino, J. Eaton, A. Mani, Comparison of Euler-Lagrange schemes in two-way coupled particle-laden channel flow, Bull. Am. Phys. Soc. (2019)
- [32] J. Horwitz, G. laccarino, J. Eaton, A. Mani, The discrete Green's function paradigm for two-way coupled Euler-Lagrange simulation, arXiv preprint, arXiv:2004.08480, 2020.
- [33] F. Battista, J.-P. Mollicone, P. Gualtieri, R. Messina, C.M. Casciola, Exact regularised point particle (ERPP) method for particle-laden wall-bounded flows in the two-way coupling regime, J. Fluid Mech. 878 (2019) 420–444.
- [34] P. Saffman, The lift on a small sphere in a slow shear flow, J. Fluid Mech. 22 (02) (1965) 385-400.
- [35] S. Rubinow, J.B. Keller, The transverse force on a spinning sphere moving in a viscous fluid, J. Fluid Mech. 11 (03) (1961) 447-459.
- [36] G. Batchelor, An Introduction to Fluid Dynamics, Cambridge University Press, 1967.
- [37] J. Finn, E. Shams, S.V. Apte, Modeling and simulation of multiple bubble entrainment and interactions with two dimensional vortical flows, Phys. Fluids 23 (2) (2011) 023301.
- [38] E. Shams, J. Finn, S. Apte, A numerical scheme for Euler–Lagrange simulation of bubbly flows in complex systems, Int. J. Numer. Methods Fluids 67 (12) (2011) 1865–1898.
- [39] D. Leith, Drag on nonspherical objects, Aerosol Sci. Technol. 6 (2) (1987) 153-161.
- [40] R.D. Moser, J. Kim, N.N. Mansour, Direct numerical simulation of turbulent channel flow up to re $\tau = 590$, Phys. Fluids 11 (4) (1999) 943–945.
- [41] A.J. Goldman, R.G. Cox, H. Brenner, Slow viscous motion of a sphere parallel to a plane wall—i motion through a quiescent fluid, Chem. Eng. Sci. 22 (4) (1967) 637–651
- [42] H. Brenner, The slow motion of a sphere through a viscous fluid towards a plane surface, Chem. Eng. Sci. 16 (3-4) (1961) 242-251.
- [43] M. Righetti, G.P. Romano, Particle-fluid interactions in a plane near-wall turbulent flow, J. Fluid Mech. 505 (2004) 93-121.
- [44] L. Zeng, F. Najjar, S. Balachandar, P. Fischer, Forces on a finite-sized particle located close to a wall in a linear shear flow, Phys. Fluids 21 (3) (2009) 033302
- [45] M.E. O'Neill, A slow motion of viscous liquid caused by a slowly moving solid sphere, Mathematika 11 (1) (1964) 67-74.
- [46] M. O'Neill, A slow motion of viscous liquid caused by a slowly moving solid sphere: an addendum, Mathematika 14 (2) (1967) 170-172.
- [47] M. Chaoui, F. Feuillebois, Creeping flow around a sphere in a shear flow close to a wall, Q. J. Mech. Appl. Math. 56 (3) (2003) 381-410.
- [48] J. Blake, A Note on the Image System for a Stokeslet in a No-Slip Boundary, Mathematical Proceedings of the Cambridge Philosophical Society, vol. 70, Cambridge University Press, 1971, pp. 303–310.
- [49] R. Clift, J.R. Grace, M.E. Weber, Bubbles, Drops, and Particles, Courier Corporation, 2005.
- [50] J. Capecelatro, O. Desjardins, An Euler-Lagrange strategy for simulating particle-laden flows, J. Comput. Phys. 238 (2013) 1-31.
- [51] P. Vasseur, R. Cox, The lateral migration of spherical particles sedimenting in a stagnant bounded fluid, J. Fluid Mech. 80 (3) (1977) 561-591.
- [52] F. Takemura, J. Magnaudet, The transverse force on clean and contaminated bubbles rising near a vertical wall at moderate Reynolds number, J. Fluid Mech. 495 (2003) 235–253.
- [53] R.G. Cox, H. Brenner, The slow motion of a sphere through a viscous fluid towards a plane surface—ii small gap widths, including inertial effects, Chem. Eng. Sci. 22 (12) (1967) 1753–1777.